

Iterative Nonlinear Beam Propagation Method and its Application in Nonlinear Devices

by

Hanhong Gao

Submitted to the Department of Electrical Engineering and Computer
Science

in partial fulfillment of the requirements for the degree of

Master of Science in Electrical Engineering and Computer Science

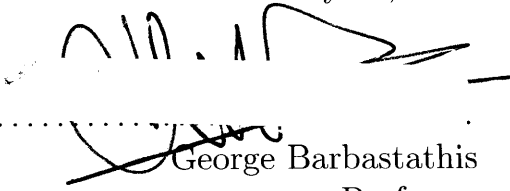
at the

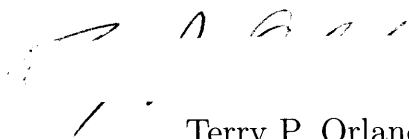
MASSACHUSETTS INSTITUTE OF TECHNOLOGY

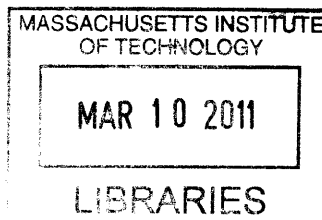
February 2011

© Massachusetts Institute of Technology 2011. All rights reserved.

Author
Department of Electrical Engineering and Computer Science
January 27, 2011

Certified by

George Barbastathis
Professor
Thesis Supervisor

Accepted by

Terry P. Orlando
Chairman, Department Committee on Graduate Theses



ARCHIVES

Iterative Nonlinear Beam Propagation Method and its Application in Nonlinear Devices

by

Hanhong Gao

Submitted to the Department of Electrical Engineering and Computer Science
on January 27, 2011, in partial fulfillment of the
requirements for the degree of
Master of Science in Electrical Engineering and Computer Science

Abstract

In this thesis, an iterative nonlinear beam propagation method is introduced and applied to optical devices. This method is based on Hamiltonian ray tracing and the Wigner distribution function. First, wave propagation simulation using Hamiltonian ray tracing is illustrated and verified with different examples. Based on this, the iterative method is presented for beam propagation in nonlinear media, which is validated with common Kerr effect phenomena such as self-focusing and spatial solitons. As the application to the analysis of nonlinear optical devices, this method is applied to nonlinear Lüneburg lens. It is found that the nonlinear Lüneburg lens is able to compensate the focal shift caused by the diffraction of Gaussian illumination.

The iterative nonlinear beam propagation method is computationally efficient and provides much physical insights into the wave propagation. Since it is based on Hamiltonian ray tracing, a ray diagram can be easily obtained which contains the evolution of generalized radiances. Besides bulk nonlinear media, this method provides a systematic approach to beam propagation problem in complex media such as nonlinear photonic crystals and metamaterials. Also, it is applicable to both coherent and partially coherent illumination. Therefore, this method has potential applications in the design and analysis of nonlinear optical devices and systems.

Thesis Supervisor: George Barbastathis

Title: Professor

Acknowledgments

First and foremost, I would like to thank the 3D Optical Systems Group. Especially, I would like to thank my thesis advisor, Professor George Barbastathis, for his patient guidance for my research. His instructions and suggestions have been greatly helpful and thought-provoking during the past one year and a half, especially when I was struggling with difficulties.

Besides, I am very grateful to my colleges (past and present) for their useful discussions, comments and kind help: Lei Tian, Baile Zhang, Satoshi Takahashi, Laura Waller, Se Baek Oh, Chih-Hao Chang, Hyungryul Choi, Justin Lee, Nick Loomis, Jonathan Petrucci, Jason Ku, Xiaogang Liu, Yi Liu, José A. Dominguez-Caballero, Yuan Luo, Se Young Yang, Aditya Bhakta, Martin Deterre, Chih-Hung Hsieh, Jeong-gil Kim, Anthony Nichol, Nader Shaar, Hyun-Jin In, Shalin Mehta, Chee Wee Tan, and Dipanjan Bhattacharya. Among them, I would especially thank Lei Tian for suggestions and discussions on how to handle different research topics, thank Baile Zhang for helping in electromagnetics, Satoshi Takahashi for instructions on MPB/MEEP simulation and nanophotonics knowledge, Laura Waller for comments on nonlinear optics and Se Baek Oh for guidance in phase space optics.

Last but not least, I would thank my wife, Yue Wu. Without her love, consideration and support, this thesis would not be possible. I would also like to thank my parents and parents-in-law for their support and love.

Contents

1	Introduction	13
1.1	Kerr nonlinearity	13
1.2	Beam propagation	14
1.3	Photonic crystals and metamaterials	15
1.4	Outline of the thesis	16
2	Introduction to Hamiltonian ray tracing	19
2.1	Screen and 3D Hamiltonian ray tracing	21
2.2	3D OPL Hamiltonian ray tracing	24
2.3	Hamiltonian ray tracing for photonic crystals	26
2.3.1	Hamiltonian ray tracing equations applied to dispersive media	27
2.3.2	2D aperiodic nanostructured Lüneburg lens	29
2.4	Effective medium theory for metamaterials	31
2.4.1	Example I: 2D subwavelength Lüneburg lens	31
2.4.2	Example II: 3D subwavelength Lüneburg lens	32
2.5	Conclusion	41
3	Hamiltonian ray tracing for wave propagation	43
3.1	Introduction to the Wigner distribution function	44
3.2	Wave propagation examples	46
3.2.1	Single and double-slit diffraction	47
3.2.2	Gaussian beams in free space	48
3.2.3	Gaussian beams in elliptical GRIN medium	51

3.2.4	Rotating beams	53
3.3	Conclusion	58
4	Iterative nonlinear beam propagation method	59
4.1	Iterative nonlinear beam propagation method	61
4.2	Examples	65
4.2.1	Self-focusing	65
4.2.2	Spatial soliton	67
4.2.3	Gaussian-Schell Model	68
4.2.4	Ray diagrams of spatial solitons	71
4.3	Conclusion	73
5	Subwavelength Lüneburg lens with nonlinear Kerr effect compensation	75
5.1	The lens equation of Lüneburg lens	76
5.2	Aperiodic subwavelength Lüneburg lens	77
5.3	Nonlinear aperiodic subwavelength Lüneburg lens	78
5.3.1	Setup	79
5.3.2	Simulation results	79
5.4	Modified aperiodic subwavelength Lüneburg lens	83
5.5	Conclusion	87

List of Figures

2-1	Geometry for screen and 3D Hamiltonian ray tracing.	21
2-2	Stiffness problem with screen Hamiltonian ray tracing numerical solver	23
2-3	Ray tracing with 3D Hamiltonian ray tracing numerical solver	24
2-4	Rays and wavefronts in Lüneburg lens with 3D OPL Hamiltonian ray tracing method	27
2-5	Unit cell of 2D aperiodic nanostructured Lüneburg lens and its dispersion diagram	30
2-6	Comparison between Hamiltonian ray tracing and FDTD results for 2D nanostructured Lüneburg lens	30
2-7	Group velocity and iso-group-velocity diagram for 2D Lüneburg lens unit cell	33
2-8	Effective refractive indices for 2D Lüneburg lens unit cells	34
2-9	Structure and FDTD results of 2D Lüneburg lens designed from dispersion relationship.	35
2-10	Sample unit cell of the 3D aperiodic subwavelength nanostructured Lüneburg lens	36
2-11	The diagram for the index retrieval method	37
2-12	Effective refractive index of unit cell of 3D Lüneburg lens regarding to the radius of silicon sphere	39
2-13	Structure and FDTD results of 3D Lüneburg lens designed from index retrieval method	40
3-1	Relationship between the WDF and initial condition of rays defined .	47

3-2	Single and double-slit diffraction	49
3-3	Electric field distribution and the WDF for the input Gaussian source	50
3-4	Gaussian beam profile while propagating in free space	51
3-5	Curve fitting results for Gaussian beam propagation in free space	52
3-6	Curve fitting results of a_1 and c_1 for Gaussian beam propagation in free space	53
3-7	Gaussian beam propagation in elliptical GRIN medium	54
3-8	Intensity and phase profiles for typical Laguerre-Gaussian modes	55
3-9	The intensity profiles of rotating beam at different propagation lengths	56
3-10	The WDF of LG (2 2) mode.	57
3-11	Rotating beam profile evolution as the beam propagates	57
3-12	Rotating beam profile evolution as the beam propagates in elliptical GRIN medium	58
4-1	Block diagram of the iterative nonlinear beam propagation method.	62
4-2	Gaussian beam profile generated from the WDF as initial condition of ray tracing	63
4-3	Optical intensity generation based on the Hamiltonian ray tracing results.	64
4-4	Periodic self-focusing of Gaussian beam in Kerr medium	66
4-5	Periodic self-focusing of two Gaussian beams in Kerr medium	67
4-6	Total intensity difference for every iteration	68
4-7	Ray tracing results from iterative nonlinear beam propagation method for spatial soliton.	69
4-8	Spatial soliton in Kerr medium	69
4-9	Gaussian-Schell model propagation in weak Kerr effect medium	71
4-10	Hamiltonian ray tracing description of spatial soliton	72
4-11	Comparison of the WDFs at different wavefront planes	73
4-12	Comparison of the intensity distribution profiles at different wavefront planes	74
5-1	The lens equation of Lüneburg lens	76

5-2	Subwavelength aperiodic nanostructured Lüneburg lens structure. . .	78
5-3	Simulation setup of nonlinear aperiodic subwavelength Lüneburg lens	79
5-4	Linear subwavelength Lüneburg lens with a Gaussian beam illumination	80
5-5	Nonlinear subwavelength Lüneburg lens with a Gaussian beam illumination	81
5-6	Effective refractive index difference between nonlinear and linear subwavelength aperiodic Lüneburg lens.	82
5-7	Relationship between focal point positions, source types and optical intensities	84
5-8	Spherical aberration minimization with the modified Lüneburg lens .	85
5-9	Rod radii distribution comparison for original and modified nonlinear Lüneburg lens.	86
5-10	Change of focus point profile for original and modified subwavelength Lüneburg lens	86

Chapter 1

Introduction

Hamiltonian optics is widely used in optical design and analysis. Hamiltonian ray tracing, a geometrical ray tracing technique based on Hamilton's equations, is very useful in analysis of optical devices and also efficient in computation. In this thesis, we introduce Hamiltonian ray tracing, take wave effects into account, and include Kerr nonlinearity by iterations with updating refractive index distribution.

1.1 Kerr nonlinearity

The Kerr effect, discovered by John Kerr in 1875, is a change in refractive index due to an applied electric field (optical intensity) [16]. All materials exhibit Kerr effect, but the main difference is their extent of the nonlinear response to the applied field. Kerr effect usually refers to two kinds of Kerr nonlinearity: the Kerr electro-optic effect and the optical Kerr effect. In this thesis, we refer to the latter.

For general nonlinearity, while applied with electric field $E(t)$, the material polarization should be written as

$$P(t) = \epsilon_0[\chi^{(1)}\mathbf{E}(t) + \chi^{(2)}\mathbf{E}^2(t) + \chi^{(3)}\mathbf{E}^3(t) + \dots], \quad (1.1)$$

where ϵ_0 is the permittivity of free space, $\chi^{(1)}$ is the linear susceptibility, and $\chi^{(2)}$ and $\chi^{(3)}$ are the second- and third-order nonlinear optical susceptibilities, respectively.

Kerr nonlinearity corresponds to the third-order susceptibility, where the refractive index changes according to the optical intensity

$$n = n_0 + \bar{n}_2 \langle \mathbf{E}^2 \rangle, \quad (1.2)$$

where n_0 is the usual refractive index and \bar{n}_2 is the second-order index of refraction, or

$$n = n_0 + n_2 I, \quad (1.3)$$

where I denotes the optical intensity.

Kerr nonlinearity results in intensity-dependent refractive index. Several phenomena are of practical importance as a result of Kerr effect. Self-focusing, self-trapping and laser beam breakup are three famous processes due to Kerr effect. Self-focusing happens when the beam intensity is so intense that the beam self-creates a waveguide and comes to focus [52]. When self-focusing and diffraction of the beam cancel each other while propagating, the beam creates a stable waveguide and is trapped in it [22]. Laser beam breakup appears as a consequence of the imperfections of the laser wavefront. Other Kerr nonlinearity phenomena include solitons [54], optical phase conjugation [109], optical bistability [42], two beam coupling [88], and so on.

In this thesis, Kerr nonlinearity is assumed for the iterative nonlinear beam propagation method. In addition, we show that Kerr nonlinearity adds one more element of design flexibility into optical devices, and nonlinearity is a parameter worth design attention.

1.2 Beam propagation

Beam propagation is an important tool in analysis of optical devices. It generally solves the Maxwell's equation [64, 55] with specific illumination under various physical objects and environment. Computational solvers and tools for the beam propagation problem include boundary element method (BEM) [8], finite-difference time-domain

method (FDTD) [57], finite element method (FEM) [95], finite integration technique (FIT) [27], uniform theory of diffraction (UTD) [56], and so on.

Nonlinearity adds one more element of design flexibility into the optical devices. Methods for beam propagation in nonlinear optical media include the split-step beam propagation method [2, 99, 90], self-consistent multimode theory [68], coherent density method [23], mutual coherence function method [86], the Wigner distribution function based method [29, 45], and so on.

1.3 Photonic crystals and metamaterials

Photonic crystals and metamaterials are two hot research topics currently. Photonic crystals are periodic nanostructures which are able to modify the behavior of light just like the affection of electron motion in semiconductor crystals [50]. It is generally classified as one-, two- and three-dimensional crystals, depending on different types of periodicity enclosed. The periodicity of the photonic crystal structure is about the same scale as half the wavelength of the light. Attractive properties of photonic crystals include three-dimensional bandgap [14], slow light [102], self-collimation [53], etc. Lots of applications have been presented so far, such as photonic crystal fibers [13], resonators [6], and omnidirectional reflectors [32].

Metamaterials [30] aim at design of artificial materials which have properties not found in the nature. It usually refers to materials with periodicity much smaller than the working wavelength of light. Metamaterials use small periodic structures to mimic large effective macroscopic behavior. Metamaterials have attracted attention from many disciplines and fields such as electromagnetics, photonics, material sciences, nanosciences, etc. Interesting applications have been reported, including superlens [60], negative refraction and perfect lens [91, 77], cloaks [84, 101, 35, 31], antennas [108], and so on.

In this thesis, Hamiltonian ray tracing for photonic crystals and metamaterials is presented. Lüneburg lens, both in 2D and 3D, is designed and verified in terms of metamaterials. Since the iterative nonlinear beam propagation method is based on

Hamiltonian ray tracing, it can be extended to the investigation of nonlinear photonic crystals and metamaterials.

1.4 Outline of the thesis

This thesis presents an iterative method for solving the nonlinear beam propagation problem. The method is based on Hamiltonian ray tracing, which makes the method physically intuitive and easy to have a radiance evolution picture. The initial condition of the ray tracing is defined by the Wigner distribution function, including the wave effects into the geometric ray tracing. The nonlinearity is used to iteratively calculate the Kerr contribution to the refractive index. This method has potential applications to nonlinear photonic crystals and metamaterials. As an example of the analysis of nonlinear optical devices, this method is applied to nonlinear Lüneburg lens. It is found that the nonlinear Lüneburg lens can compensate the focal shift caused by the diffraction of Gaussian illumination.

In Chapter 2, general Hamiltonian ray tracing is introduced. It is extended to 3D Hamiltonian ray tracing based on the optical path length. In addition, an introduction to Hamiltonian ray tracing applied to photonic crystals and metamaterials has been made. What's more, effective medium theory for analysis of metamaterials is briefly described and applied to the design of Lüneburg lens.

In Chapter 3, Hamiltonian ray tracing is applied to the analysis of wave propagation, by defining its initial condition through the Wigner distribution function. This method includes wave effects into geometrical ray tracing. It is verified with examples such as single and double-slit diffraction, and the propagation of Gaussian beams and rotating beams.

In Chapter 4, the iterative nonlinear beam propagation method is presented in detail. A comparison to the split-step beam propagation method has been made. In addition, the method is validated with common Kerr effect phenomena such as self-focusing, spatial soliton and Gaussian-Schell model propagation.

In Chapter 5, the iterative method is applied to nonlinear Lüneburg lens. The

compensation of focal shift due to the competition between nonlinearity and diffraction is discussed. Also, a modified Lüneburg lens is designed to minimize the spherical aberration caused by the nonlinearity.

Chapter 2

Introduction to Hamiltonian ray tracing

Ray tracing is a general path generation method for waves or particles through media or systems with a conservative (Hamiltonian) potential. It has been widely used in research fields such as under water acoustics [41], seismology [100], plasma physics [20], radio physics [65], optics [93], and so on. In optics, especially in optical design and engineering, ray tracing is widely used. For example, optical design software such as ZEMAX is based on ray tracing for design of optical systems. Ray tracing is especially helpful in design and analysis of GRadient-INdex (GRIN) optical devices. GRIN lens [70] has a gradually changing refractive index distribution such that optical rays will follow curves instead of straight lines. Ray tracing provides an approximate solution to the Maxwell's equations, under the assumption that the dimensions of the objects are much greater than the wavelength.

Assuming that GRIN has a refractive index profile $n(\mathbf{r})$, the path of rays is governed by the ray equation [15, 85]

$$\frac{d}{ds} \left[n(\mathbf{r}) \frac{d\mathbf{r}}{ds} \right] = \nabla n(\mathbf{r}), \quad (2.1)$$

where $n(\mathbf{r})$ denotes the refractive index at position \mathbf{r} , s parameterizes the ray trajectory. Many ray tracing techniques have been presented and applied, including

ray tracing in cylindrical coordinates [79], analytical ray tracing method [62, 63], polynomial solution of the differential equation method [69] and so on. For most of the existing methods, derived ray tracing equations are solved through standard numerical techniques such as the Runge-Kutta method [82].

Hamiltonian ray tracing [19, 107] is based on Fermat's extremal principle [46]. Ray trajectories satisfy Hamiltonian equations originated from Lagrangian and Fermat's principle. The Hamiltonian expresses momentum conservation in this case. This type of ray tracing has been chosen as a main topic in the discussions of this Chapter.

With the research and application development in photonic crystals and metamaterials, beam propagation in these media is of great importance [73, 1]. A conventional treatment for this problem is finite-difference time-domain (FDTD) method [104]. However, ray tracing is usually computationally more efficient than FDTD [49]. Hamiltonian ray tracing has been extended to photonic crystals [81, 49] for fast and reliant beam propagation analysis.

As for metamaterials, they are always treated as effective media since the operational optical wavelength is much larger than the unit cell, thus the corresponding effective refractive index distribution can be generated. In this way, an analogy is made between metamaterials and the corresponding GRIN media [58, 110]. GRIN media ray tracing sheds light on the analysis of metamaterials.

In this Chapter, Hamiltonian ray tracing is briefly introduced in terms of screen and 3D Hamiltonian ray tracing. Due to their numerical limitations, 3D Hamiltonian ray tracing method based on optical path length is introduced as an extension. Also, Hamiltonian ray tracing equations applicable for photonic crystals are presented and proved that they are equivalent to the original 3D Hamiltonian equations. Finally, effective medium theory for analysis of metamaterials is briefly described and examples are given as 2D and 3D Lüneburg lens.

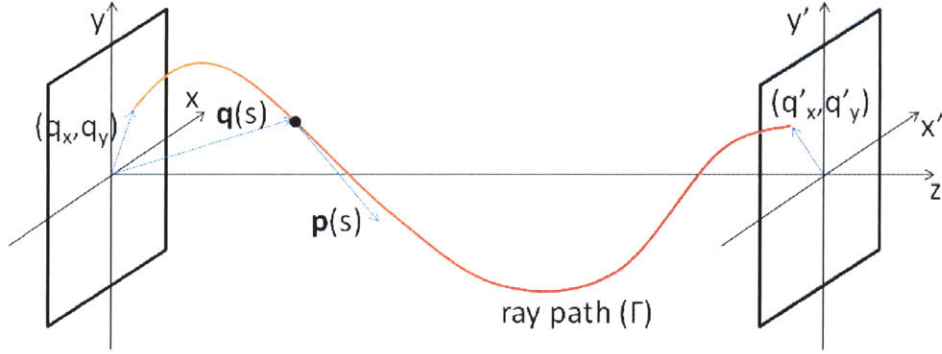


Figure 2-1: Geometry for screen and 3D Hamiltonian ray tracing.

2.1 Screen and 3D Hamiltonian ray tracing

Hamiltonian ray tracing [19, 107] originates from Fermat's extremal principle and is applicable to both isotropic and anisotropic media [80]. Conventionally it has two forms, namely screen Hamiltonian and three-dimensional (3D) Hamiltonian. In this section a brief introduction to both of them will be made.

Geometry for Hamiltonian ray tracing is shown above in Fig. 2-1. The main difference between the two representations is the parameter to represent the ray trajectory. While screen Hamiltonian uses the optical axis z and leaves x and y as coordinates on the "screen", 3D Hamiltonian uses on-trajectory parameter s and keeps all three coordinate directions as the representation of positions and momenta.

Fermat's principle defines the optical path length (OPL) as

$$\mathcal{L} \equiv \int_{\Gamma} n(\mathbf{q}) dl, \quad (2.2)$$

where Γ is the ray path and dl is the elemental arc length along Γ . Note that $\mathbf{q} \equiv (q_x, q_y, q_z)$ is used as a symbol for position and $\mathbf{p} \equiv (p_x, p_y, p_z)$ is used as a symbol for momentum.

For screen Hamiltonian, position and momentum are defined on $x-y$ screens thus they are a function of z :

$$\mathbf{q}(z) = (q_x(z), q_y(z)); \quad \mathbf{p}(z) = (p_x(z), p_y(z)). \quad (2.3)$$

In this way, OPL can be written as

$$\mathcal{L} = \int_{z_1}^{z_2} L(\mathbf{q}, \dot{\mathbf{q}}, z) dz = \int_{z_1}^{z_2} n(\mathbf{q}, z) \sqrt{|\dot{\mathbf{q}}|^2 + 1} dz, \quad (2.4)$$

where $L(\mathbf{q}, \dot{\mathbf{q}}, z)$ is optical Lagrangian, $\dot{\mathbf{q}}(z) = (dx/dz, dy/dz)$ and z_1, z_2 denote the initial and final z “screens” for the trajectory.

As for all Lagrangians, optical Lagrangian should satisfy Euler’s equation

$$\frac{\partial L}{\partial \mathbf{q}} - \frac{d}{dz} \frac{\partial L}{\partial \dot{\mathbf{q}}} = 0. \quad (2.5)$$

From here, by using Legendre transform

$$H \equiv \mathbf{p} \cdot \dot{\mathbf{q}} - L \quad (2.6)$$

to substitute Lagrangian L by Hamiltonian H , finally we can get the screen Hamiltonian equations

$$\dot{\mathbf{q}} = \frac{\partial H}{\partial \mathbf{p}} = -\frac{\mathbf{p}}{H}, \quad \dot{\mathbf{p}} = -\frac{\partial H}{\partial \mathbf{q}} = -\frac{n}{H} \frac{\partial n}{\partial \mathbf{q}}, \quad (2.7)$$

where

$$H = -\sqrt{n^2(\mathbf{q}, z) - |\mathbf{p}|^2} = -p_z. \quad (2.8)$$

Physical meaning for screen Hamiltonian H is negative value of the z component of momentum \mathbf{p} . With Hamiltonian equations on hand, ray trajectory could be solved by numerical method such as “ODE45” in MATLAB® which uses the explicit Runge-Kutta (4,5) formula.

However, a potential drawback makes this method a bit troublesome. By default, ODE45 calculates towards $+z$ direction. If there is any chance the ray should go around and travel backwards at $-z$ direction, this method might fail. For example, Fig. 2-2 shows ray tracing results from screen Hamiltonian with cylindrically symmetric refractive index distribution $n(r) \sim 1/r$. Theoretically the ray should rotate

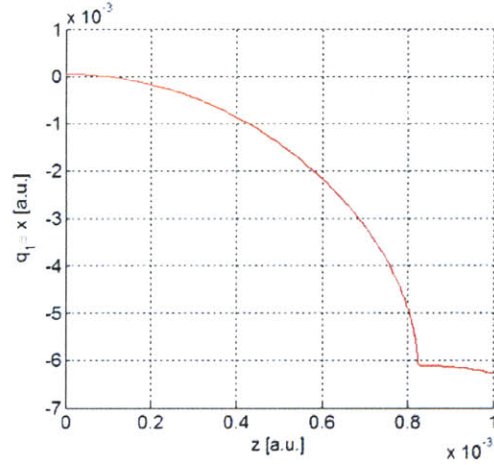


Figure 2-2: Stiffness problem with screen Hamiltonian ray tracing numerical solver when ray direction is almost vertical to the optical axis. Here refractive index distribution follows $n(r) \sim 1/r$.

but it can be seen in Fig. 2-2 that when ray is almost vertical to optical axis, the method crashes since numerical solver needs infinite small calculation step in z . This is called stiffness problem [94] of “ODE” solver.

This problem can be avoided when 3D Hamiltonian ray tracing equations are used. 3D Hamiltonian uses s to parameterize the ray trajectory so

$$\mathbf{q}(s) = (q_x(s), q_y(s), q_z(s)); \quad \mathbf{p}(s) = (p_x(s), p_y(s), p_z(s)). \quad (2.9)$$

Thus optical Lagrangian in this case is

$$L(\mathbf{q}, \dot{\mathbf{q}}, s) = n(\mathbf{q})|\dot{\mathbf{q}}| \quad (2.10)$$

where $\dot{\mathbf{q}}(s) = (dx/ds, dy/ds, dz/ds)$ and $(ds)^2 = (dx)^2 + (dy)^2 + (dz)^2$.

By following the similar derivation as previous, 3D Hamiltonian equations can be given as

$$\frac{d\mathbf{q}}{ds} = \frac{\partial H}{\partial \mathbf{p}} = \frac{\mathbf{p}}{|\mathbf{p}|}, \quad \frac{d\mathbf{p}}{ds} = -\frac{\partial H}{\partial \mathbf{q}} = \frac{\partial n}{\partial \mathbf{q}}, \quad (2.11)$$

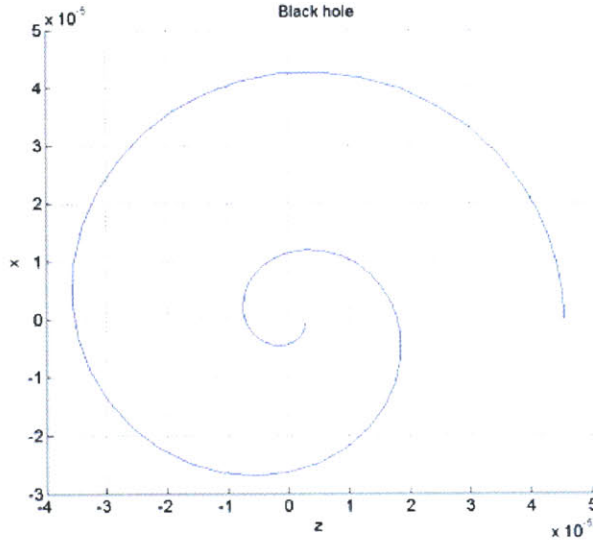


Figure 2-3: Ray tracing with 3D Hamiltonian ray tracing numerical solver. Here refractive index distribution follows $n(r) \sim 1/r$.

where

$$H = |\mathbf{p}| - n(\mathbf{q}). \quad (2.12)$$

Again, this method is applied to the “black hole” refractive index distribution and results are shown in the following Fig. 2-3. As expected, the ray rotates as it approaches the “potential center”. With this ray tracing method, stiffness problem as mentioned above is solved. The very reason 3D Hamiltonian ray tracing does not have this problem is that ray is always propagating towards the $+s$ direction. This is how s is defined and it exactly meets the need of the numerical solver.

2.2 3D OPL Hamiltonian ray tracing

In this section, the 3D Hamiltonian ray tracing has been extended to 3D OPL Hamiltonian ray tracing, in order to facilitate the generation of wavefronts and provide more physical insight. As has been introduced in the previous section, 3D Hamiltonian ray tracing uses s to parameterize the actual ray path. However, the optics, a

more intuitive way to denote the ray path is to use OPL. With OPL, the wavefronts can be easily generated numerically based on the ray tracing results. The governing equations of 3D OPL Hamiltonian ray tracing are derived as follows.

Instead of using s , $s' = n(\mathbf{q})s$ is used to parameterize the ray path. The OPL becomes

$$\mathcal{L} = \int_{s'_1}^{s'_2} n \sqrt{\left(\frac{dx}{ds'}\right)^2 + \left(\frac{dy}{ds'}\right)^2 + \left(\frac{dz}{ds'}\right)^2} ds'. \quad (2.13)$$

The optical Lagrangian changes into

$$L = n|\dot{\mathbf{q}}|, \quad (2.14)$$

where

$$\dot{\mathbf{q}} = \left(\frac{dx}{ds'}, \frac{dy}{ds'}, \frac{dz}{ds'}\right) = \frac{1}{n} \left(\frac{dx}{ds}, \frac{dy}{ds}, \frac{dz}{ds}\right). \quad (2.15)$$

Therefore

$$|\dot{\mathbf{q}}| = \frac{1}{n}, \quad L = 1. \quad (2.16)$$

The momentum can be expressed as

$$\mathbf{p} = \frac{\partial L}{\partial \dot{\mathbf{q}}} = n \frac{\dot{\mathbf{q}}}{|\dot{\mathbf{q}}|}, \quad (2.17)$$

from which

$$|\mathbf{p}| = n. \quad (2.18)$$

Thus

$$\dot{\mathbf{q}} = \frac{\mathbf{p} \cdot |\dot{\mathbf{q}}|}{n} = \frac{\mathbf{p}}{n|\mathbf{p}|}, \quad (2.19)$$

using Eq. 2.16 and Eq. 2.18.

3D Hamiltonian under OPL is defined through Legendre transformation:

$$H = \mathbf{p} \cdot \dot{\mathbf{q}} - L = \mathbf{p} \cdot \frac{\mathbf{p}}{n|\mathbf{p}|} - 1 = \frac{|\mathbf{p}|}{n} - 1, \quad (2.20)$$

using Eq. 2.16.

Thus Hamiltonian equations are:

$$\frac{d\mathbf{q}}{ds'} = \frac{\partial H}{\partial \mathbf{p}} = \frac{1}{n} \frac{\mathbf{p}}{|\mathbf{p}|}, \quad (2.21)$$

$$\frac{d\mathbf{p}}{ds'} = -\frac{\partial H}{\partial \mathbf{q}} = \frac{1}{n} \frac{\partial n}{\partial \mathbf{q}}. \quad (2.22)$$

The 3D OPL Hamiltonian ray tracing is different with original 3D Hamiltonian ray tracing only in the scaling factor $1/n$, since s' has been scaled by $n(\mathbf{q})$. The advantage of using this method is for easier generation of wavefronts. Besides, the numerical results are physically more intuitive.

Here a Lüneburg lens with radius 1 and refractive index distribution $n = \sqrt{2 - r^2}$ is taken as an example. Ambient material refractive index $n_0 = 1$. Lüneburg lens could focus a plane wave to an ideal geometric point at the opposite of the lens [61]. The ray tracing results (blue lines) as well as the wavefronts (green lines) obtained with ODE45 in MATLAB® are shown in Fig. 2-4. It can be observed that a plane wave is focused at the right edge and all the rays hitting the focus point are of the same OPL. This is exactly the property of a Lüneburg lens. Here wavefronts are easily generated by connecting all the points in all the rays with the same s' value.

2.3 Hamiltonian ray tracing for photonic crystals

Solving the two coupled differential Hamiltonian equations is very fast with standard numerical solvers such as Runge-Kutta. Therefore ray tracing is very promising if it could be applied to photonic crystals with adiabatically variant periodicity. Conventional treatment of beam propagation in photonic crystal is the FDTD method. However, it is not computationally efficient. It has been proven that Hamiltonian optics can be applied to photonic crystals by incorporating the dispersion relation of the unit cells [81, 49]. Hamiltonian ray tracing is computationally more efficient comparing with FDTD method and also ray tracing provides more physical insights into the beam propagation and energy evolution in photonic crystals.

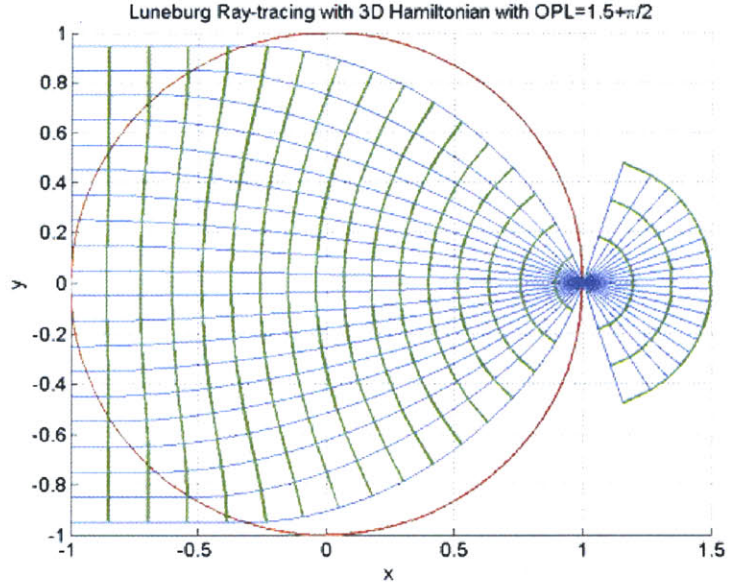


Figure 2-4: Rays and wavefronts in Lüneburg lens with 3D OPL Hamiltonian ray tracing method. Plane wave is illuminating from the left. Blue lines are rays and green lines are wavefronts.

2.3.1 Hamiltonian ray tracing equations applied to dispersive media

For photonic crystals, Hamiltonian ray tracing equations can be written as [49]

$$\frac{d\mathbf{q}}{dt} = \frac{\partial\omega(\mathbf{q}, \mathbf{k})}{\partial\mathbf{k}}, \quad \frac{d\mathbf{k}}{dt} = -\frac{\partial\omega(\mathbf{q}, \mathbf{k})}{\partial\mathbf{q}}, \quad (2.23)$$

where $\omega(\mathbf{q}, \mathbf{k})$ is the dispersion relation, \mathbf{k} is the wave vector, \mathbf{q} is position, and t is time.

In this subsection, the relationship between Eq. 2.23 and 3D Hamiltonian ray tracing equations (Eq. 2.11) is discussed. Throughout this subsection, when the equations from Ref. [9] and Ref. [10] are cited, a notation change has been deployed to make them consistent with the notation used in this thesis:

$$\mathbf{r} \rightarrow \mathbf{q}, \quad p \rightarrow s, \quad k \rightarrow \frac{n}{c}\omega, \quad \mathbf{q} \rightarrow \frac{\omega}{c}\mathbf{p},$$

while Hamiltonian $H = |\mathbf{p}| - n = 0$.

We begin the discussion from the transport equation for the Wigner distribution function. It has been shown by Bastiaans that the Wigner distribution function follows the ray tracing path governed by the Hamiltonian equations (Eq. 29 of Ref. [9]):

$$\frac{d\mathbf{q}}{ds} = \frac{\mathbf{p}}{n}, \quad \frac{d\mathbf{p}}{ds} = \frac{\partial n}{\partial \mathbf{q}}, \quad (2.24)$$

which are 3D Hamiltonian equations.

Also, from Eq. 24 of Ref. [9]:

$$\frac{d\mathbf{q}}{dz} = \frac{\mathbf{p}}{\sqrt{n^2 - |\mathbf{p}|^2}}, \quad \frac{d\mathbf{p}}{dz} = \frac{n}{\sqrt{n^2 - |\mathbf{p}|^2}} \frac{\partial n}{\partial \mathbf{q}} \quad (2.25)$$

which are screen Hamiltonian equations.

For photonic crystals, the medium is inhomogeneous and dispersive, meaning that refractive index can be expressed as $n = n(\mathbf{q}, \mathbf{p}, t, \omega)$. From Eq. 30 and Eq. 42 of Ref. [10],

$$\frac{d\mathbf{q}}{dt} = \frac{\partial \Omega}{\partial \mathbf{k}}, \quad \frac{d\mathbf{k}}{dt} = -\frac{\partial \Omega}{\partial \mathbf{q}}, \quad \frac{d\omega}{dt} = \frac{\partial \Omega}{\partial t}. \quad (2.26)$$

where $\omega = \Omega(\mathbf{q}, \mathbf{k}, t)$. These equations are consistent with Eq. 2.23.

Equivalently in Eq. 42 of Ref. [10]:

$$\frac{d\mathbf{q}}{dt} = \frac{c}{\omega} \frac{\partial \Omega}{\partial \mathbf{p}} = \left(\frac{\mathbf{p}}{n} - \frac{\partial n}{\partial \mathbf{p}} \right) / \left(\frac{n}{c} + \frac{\omega}{c} \frac{\partial n}{\partial \omega} \right), \quad (2.27)$$

$$\frac{\omega}{c} \frac{d\mathbf{p}}{dt} = -\frac{\partial \Omega}{\partial \mathbf{q}} = \frac{\partial n}{\partial \mathbf{q}} \left(\frac{n}{c} + \frac{\omega}{c} \frac{\partial n}{\partial \omega} \right). \quad (2.28)$$

When the medium under investigation is homogeneous in time and does not exhibit dispersion for spatial frequency variable, refractive index is $n = n(\mathbf{r}, \omega)$. In this case, Eq. 2.27 can be reduced to (Eq. 43 of Ref. [10])

$$\frac{d\mathbf{q}}{dt} = \frac{\mathbf{p}}{n} / \left(\frac{n}{c} + \frac{\omega}{c} \frac{\partial n}{\partial \omega} \right). \quad (2.29)$$

This is equivalent to (Eq. 45 of Ref. [10])

$$\frac{d\mathbf{q}}{ds} = \frac{\mathbf{p}}{n}, \quad \frac{d\mathbf{p}}{ds} = \frac{\partial n}{\partial \mathbf{q}}. \quad (2.30)$$

by parameterize using s instead of t . This is exactly 3D Hamiltonian ray tracing equations.

Therefore, it has been shown that Hamiltonian equations used for photonic crystals are equivalent to 3D Hamiltonian equations.

2.3.2 2D aperiodic nanostructured Lüneburg lens

Lüneburg lens [61] is a gradient-index device with refractive index distribution $n(r) = n_0\sqrt{2 - (r/R)^2}$, where n_0 is the refractive index of the medium outside the lens, R is the radius of lens, and r is the distance to the center of the lens. It can focus a plane wave illumination to a perfect geometric focus point at the opposite edge of the lens. In this subsection a 2D aperiodic nanostructured Lüneburg lens [97] is used as an example of application of the Hamiltonian ray tracing method for photonic crystals.

The lens structure is similar to the one shown in Fig. 2-9(a), which consists of unit cells with silicon rods embedded in air (See Fig. 2-5(a)). Its dispersion relation is shown in Fig. 2-5(b). The rod radii profile of the Lüneburg lens is $a(r) = a_1\sqrt{2 - (r/R)^2} + a_2$, where $a_1 = 0.367a_0$, $a_2 = -0.101a_0$ and $R = 30a_0$. The free space wavelength used is $\lambda = 1550$ nm.

Ray tracing is numerically implemented by solving Eq. 2.23 with the Runge-Kutta method. For every position of the lens, the dispersion relation is known and Eq. 2.23 can be solved. The results are shown in Fig. 2-6 with a comparison to results obtained from conventional FDTD method. A good agreement can be seen. The illuminating plane wave is focused on the opposite edge of the lens. Therefore, Hamiltonian ray tracing is applicable to photonic crystals.

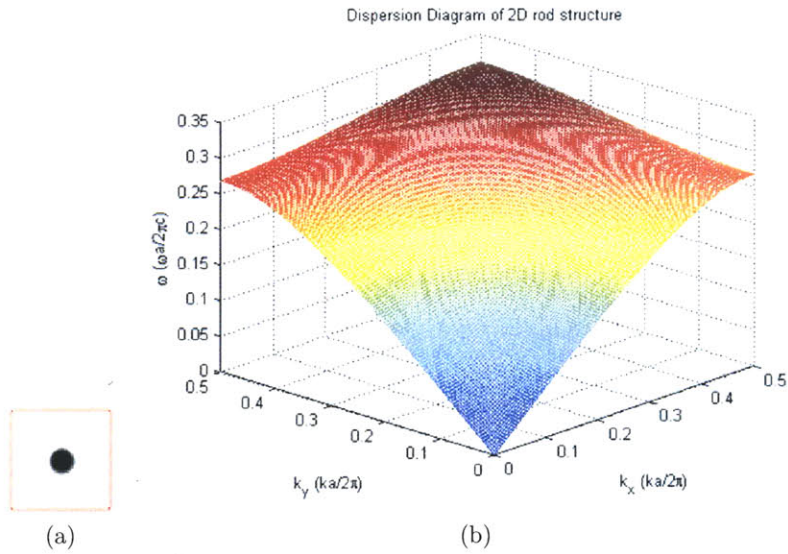


Figure 2-5: Unit cell of 2D aperiodic nanostructured Luneburg lens (a) and its dispersion diagram.

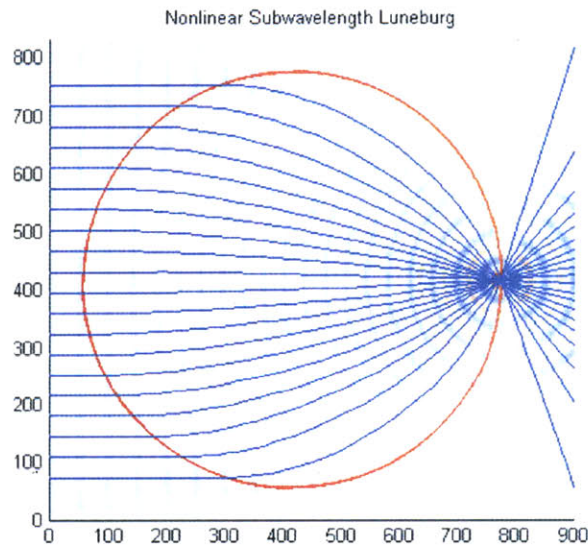


Figure 2-6: Comparison between Hamiltonian ray tracing and FDTD results for 2D nanostructured Luneburg lens. Red circle encloses the lens. Blue lines are ray tracing results. Red and dark blue color shading denotes the electric field distribution.

2.4 Effective medium theory for metamaterials

Research in metamaterials is fast-developing and beam propagation analysis is becoming more and more important. Ray tracing again can be very useful in analysis of metamaterials. Most metamaterials are operated under wavelength which is much longer than the size of unit cell of the metamaterials. Therefore, these metamaterials can be treated as a GRIN lens, homogeneous or inhomogeneous, isotropic or anisotropic. Ray tracing can be calculated according to the effective GRIN lens. In this way, the key problem is: given a unit cell and operation wavelength, what is the effective refractive index of the unit cell?

In this section, different methods for effective refractive index calculation have been presented and compared. Two examples, aperiodic subwavelength nanostructured Lüneburg lenses both in 2D and in 3D, are designed with effective medium theory. For illustration purposes, our examples are solely inhomogeneous and isotropic. Extending this method to anisotropic metamaterials are straight-forward since Hamiltonian equations have been extended to anisotropic media [80].

2.4.1 Example I: 2D subwavelength Lüneburg lens

Lüneburg lens as a GRIN lens is not achievable as a bulk medium. Here an aperiodic subwavelength nanostructure is designed to mimic the refractive index profile. Here we assume transverse-electric (TE) wave where electric field is perpendicular to the 2D plane.

We revisit the subwavelength Lüneburg lens mentioned in the previous section. The unit cell consists of a silicon rod ($n = 3.46$) in air ($n = 1$). Free space wavelength is $\lambda = 1550 \text{ nm} = 8a$. Two methods are used to generate the effective refractive index.

(1) Analytical method.

For TE mode, effective refractive index could be expressed analytically as [87]

$$\epsilon_{eff} = f \cdot \epsilon_1 + (1 - f) \cdot \epsilon_0, \quad (2.31)$$

where f is the filling factor of the silicon rod in terms of area, ϵ_1 and ϵ_0 correspond to the permittivity of the rod and air, respectively.

(2) Dispersion diagram method.

According to the dispersion diagram for this unit cell described in the previous section, group velocities at different wave vector \mathbf{k} can be calculated with group velocity definition

$$\mathbf{v}_g = \frac{\partial \omega(\mathbf{k})}{\partial \mathbf{k}}. \quad (2.32)$$

The results are shown in Fig. 2-7(a). Iso-group-velocity contours are also illustrated as in Fig. 2-7(b). For the wavelength chosen in this case, $|\mathbf{k}|a/2\pi = 1/8$. For such a small \mathbf{k} , iso-group-velocity contour is almost a circle, meaning that this structure should be isotropic. Based on these, the effective refractive index is calculated by

$$n_{eff} = c/|\mathbf{v}_g|, \quad (2.33)$$

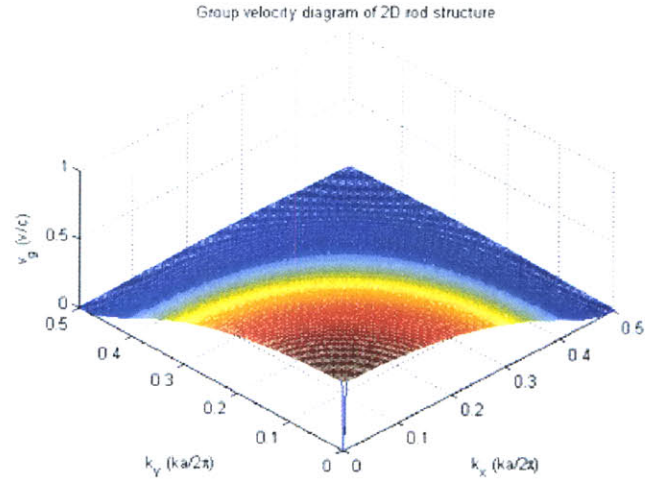
where c is the free space speed of light.

Effective indices for different radii of rods calculated from both methods above are illustrated in Fig. 2-8. Two methods give close effective indices.

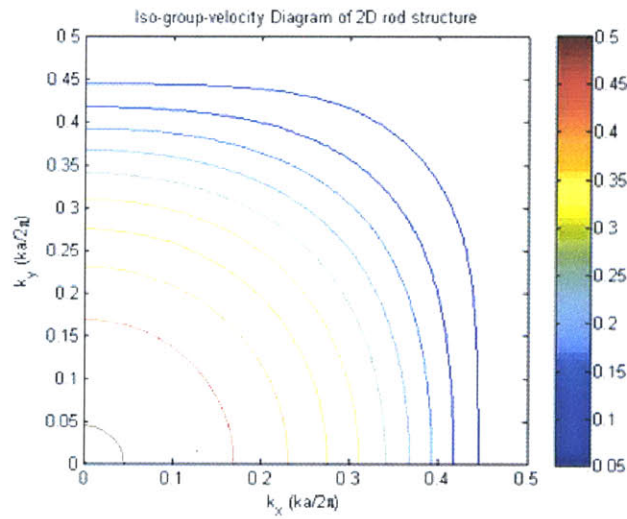
A 2D Lüneburg lens has been designed and verified based on method (1). Here, based on the effective refractive indices, a 2D subwavelength Lüneburg lens is designed with effective refractive index ranging from 2 to $2\sqrt{2}$. The structure and FDTD results are shown in Fig. 2-9. It can be seen that a plane wave is focused at the opposite of the lens.

2.4.2 Example II: 3D subwavelength Lüneburg lens

Effective refractive index calculation for three-dimensional unit cell is a more interesting topic. A typical unit cell structure is shown in Fig. 2-10, where a spherical silicon ball ($n = 3.46$) is embedded at the very center of a cubic air ($n = 1$) cell.



(a)



(b)

Figure 2-7: Group velocity as a function of wave vector \mathbf{k} (a) and iso-group-velocity diagram (b) for the unit cell of aperiodic subwavelength nanostructured Lüneburg lens.

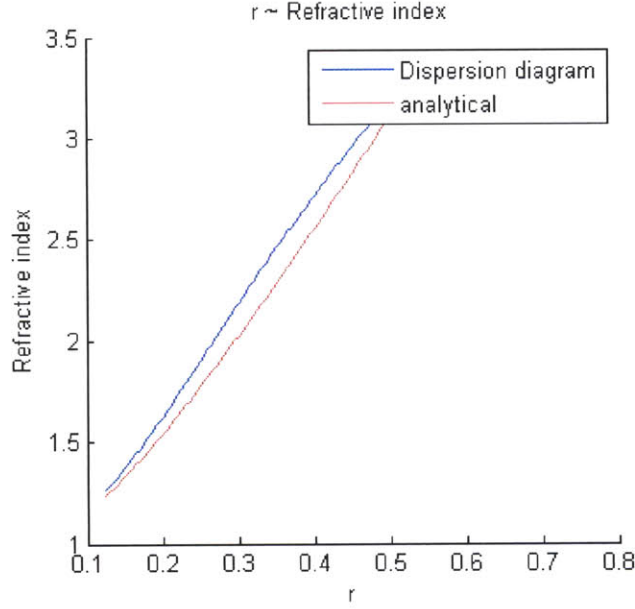


Figure 2-8: Effective refractive indices at different radii of rods for the unit cells of aperiodic subwavelength nanostructured Lüneburg lens.

Many methods have been developed to calculate the effective refractive index, namely effective medium approximations. Among them, there are:

- (1) Maxwell-Garnett equations [40].

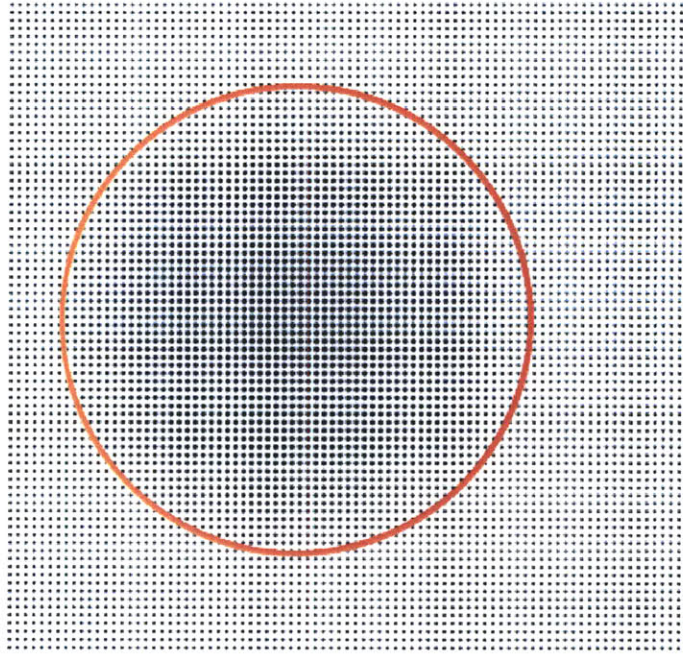
Maxwell-Garnett equations, as well as Bruggeman equations which will be introduced later, are two kinds of effect medium theory which are widely used [48]. They relate the effective permittivity ϵ_{eff} of a unit cell which consists of two materials, to the permittivities of the two materials. Maxwell-Garnett equations have two forms:

$$\left(\frac{\epsilon - \epsilon_1}{\epsilon + 2\epsilon_1} \right) = \eta_0 \left(\frac{\epsilon_0 - \epsilon_1}{\epsilon_0 + 2\epsilon_1} \right), \quad (2.34)$$

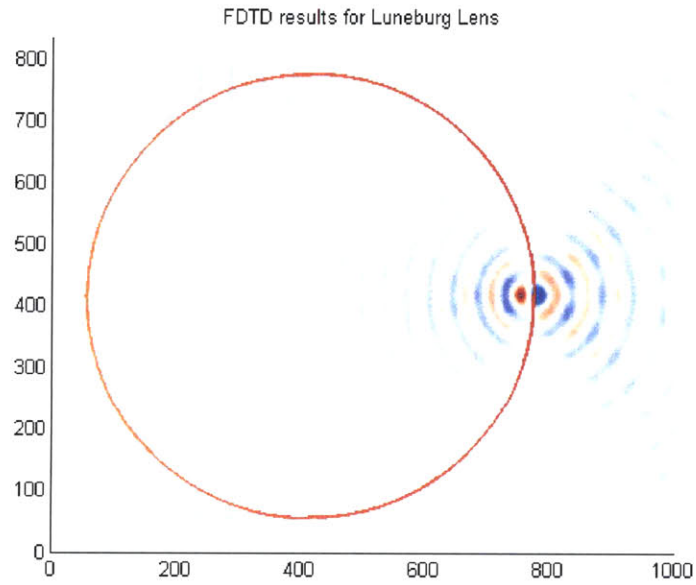
$$\left(\frac{\epsilon - \epsilon_0}{\epsilon + 2\epsilon_0} \right) = \eta_1 \left(\frac{\epsilon_1 - \epsilon_0}{\epsilon_1 + 2\epsilon_0} \right), \quad (2.35)$$

where ϵ_0 and ϵ_1 are the permittivities of air and silicon, and η_0 and η_1 are the filling factors in volume of air and silicon, respectively.

Eq. 2.34 treats air as an ambient material and silicon sphere as inclusion, while for



(a)



(b)

Figure 2-9: Structure (a) and FDTD results (b) of 2D aperiodic subwavelength nanostructured Luneburg lens, whose effective refractive indices are calculated from dispersion relations. Effective refractive index ranges from 2 to $2\sqrt{2}$.

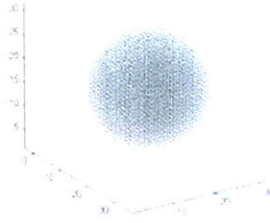


Figure 2-10: Sample unit cell of the 3D aperiodic subwavelength nanostructured Lüneburg lens, where size of the unit cell is $a_0 = 32$.

Eq. 2.35, it treats silicon as ambient material and air as inclusion. Maxwell-Garnett equations are expected to be valid when the volume fraction η is small, since it is assumed that the two materials are spatially separated.

(2) Bruggeman equations [18].

Bruggeman equations are another way to make an approximation of effective refractive index. Bruggeman equations take the form of

$$\eta_1 \left(\frac{\epsilon_1 - \epsilon}{\epsilon_1 + 2\epsilon} \right) + \eta_2 \left(\frac{\epsilon_2 - \epsilon}{\epsilon_2 + 2\epsilon} \right) = 0, \quad (2.36)$$

where ϵ_1 and ϵ_2 are the permittivities of air and silicon, and η_1 and η_2 are the filling factors in volume of air and silicon, respectively.

Unlike Maxwell-Garnett equations, Bruggeman equations make no assumptions on the filling factor thus they treat air and silicon equally. While the permittivities of two materials are close to each other, it is assumed that Bruggeman equations provide a valid approximation.

(3) Dispersion diagram method.

The same as in the 2D case, dispersion diagram method can also be applied to 3D case. Dispersion diagram relating the frequency $\omega(\mathbf{k})$ to the wave vector \mathbf{k} for the different unit cells can be calculated. For a particular silicon sphere radius and operation wavelength, group velocity can be found. Since here we again assume that wavelength is much longer than the size of the unit cell, the material could be treated as isotropic. Effective refractive index for certain unit cell can be found from the group velocity.

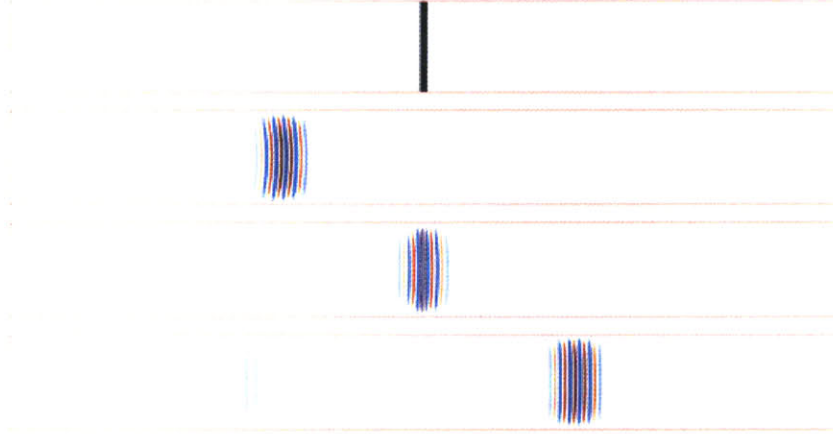


Figure 2-11: The diagram for the index retrieval method. First row is the simulation setup. Second row shows a Gaussian pulse illumination. Third row gives the Gaussian pulse hitting on the metamaterial layer. Last row shows one transmission and one reflection Gaussian pulse. See text for details.

(4) Index retrieval method [92, 21].

Index retrieval method has been widely used as a reliable way to calculate the effective permittivity and permeability of metamaterials. It takes advantage of the reflection and transmission data, i.e. S_{11} and S_{21} in transmission matrix. The diagram for index retrieval method is illustrated in Fig. 2-11. A Gaussian pulse is passing through a layer of the metamaterial, resulting into a transmission pulse and a reflection pulse. Assuming that this layer consists of homogeneous material, with effective permittivity and permeability we are seeking, instead of layer of metamaterial, the transmission pulse and reflection pulse should be the same with metamaterial case. In this way, scattering parameters S_{11} and S_{21} could be expressed as

$$S_{11} = \frac{R_{01}(1 - e^{i2nk_0d})}{1 - R_{01}^2 e^{i2nk_0d}}, \quad (2.37)$$

$$S_{21} = \frac{(1 - R_{01}^2)e^{ink_0d}}{1 - R_{01}^2 e^{i2nk_0d}}, \quad (2.38)$$

where $R_{01} = (z - 1)/(z + 1)$. Here z is the characteristic impedance, n is the effective refractive index, k_0 is the free-space wave vector and d is the thickness of slab.

In this way, index retrieval method can be performed as following. Firstly, the slab of metamaterial we are investigating is placed with illumination of the Gaussian pulse. Simulation such as FDTD is applied to obtain the transmission and reflection pulses. Scattering parameters are thus calculated. Effective impedance and refractive index is calculated by the following equations obtained by reverting Eq. 2.37 and Eq. 2.38:

$$z = \pm \sqrt{\frac{(1 + S_{11})^2 - S_{21}^2}{(1 - S_{11})^2 - S_{21}^2}}, \quad (2.39)$$

$$e^{ink_0d} = X \pm i\sqrt{1 - X^2}, \quad (2.40)$$

where $X = 1/2S_{21}(1 - S_{11}^2 + S_{21}^2)$. Thus effective permittivity and permeability can be obtained from the retrieved values of z and n .

In order to design a 3D Lüneburg lens, relationship between the radius of silicon sphere in Fig. 2-10 and effective refractive index is calculated and shown in Fig. 2-12.

From the figure it can be seen that two types of Maxwell-Garnett equations offer upper and lower limits for the effective refractive index of a typical unit cell. They almost overlap when radius of silicon sphere is small enough, which matches our discussion above. Results provided by Bruggeman does not make any sense; for radius of sphere smaller than 0.32, the refractive index does not exist. This is because the refractive indices of air and silicon have a huge difference. Dispersion relation diagram and index retrieval method give mostly the similar results.

Three-dimensional Lüneburg lens is designed with effective refractive index calculated from index retrieval method, with effective refractive index ranging from 1.1 to $1.1 \times \sqrt{2}$. Due to memory limit, only one layer of unit cells is simulated. A slice along the plane is made to show the sphere ball distribution (Fig. 2-13(a)). From Fig. 2-13(b) it can be seen that a plane wave has been focused at the right edge of the lens.

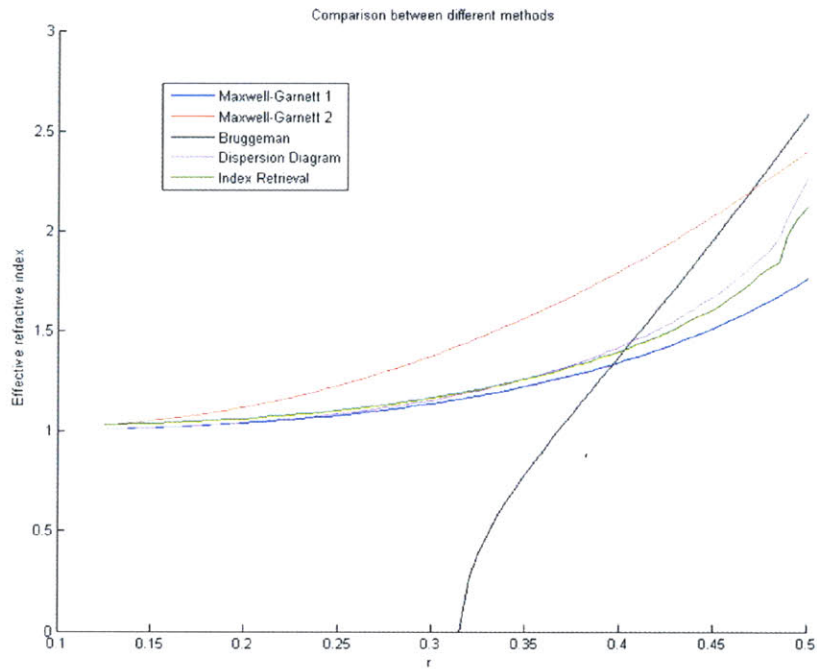
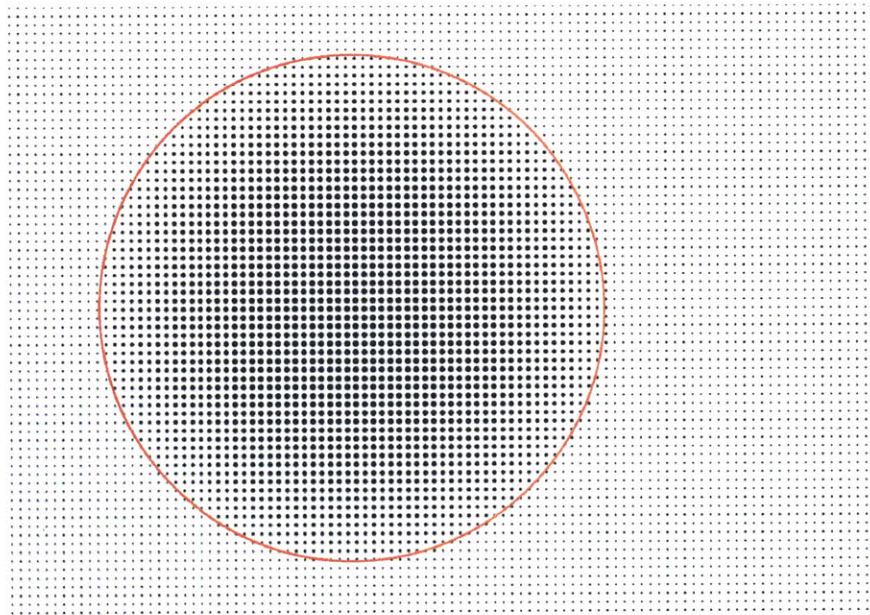
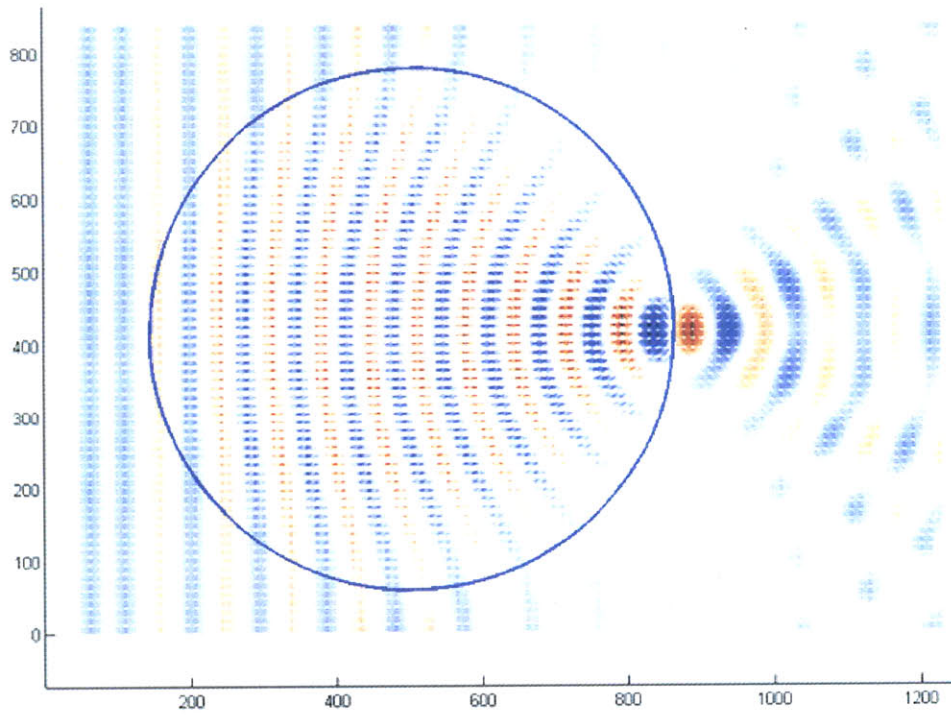


Figure 2-12: Effective refractive index of unit cell of 3D Luneburg lens regarding to the radius of silicon sphere. Four methods are used, including Maxwell-Garnett equations (Types I and II), Bruggeman equations, dispersion relation diagram, and index retrieval method. See text for more details.



(a)



(b)

Figure 2-13: Structure (a) and FDTD results (b) of 3D aperiodic subwavelength nanostructured Lüneburg lens, whose effective refractive indices are calculated from index retrieval method. Effective refractive index ranges from 1.1 to $1.1 \times \sqrt{2}$. Red and blue lines denote the Lüneburg lens. Red and dark blue color shading denotes the electric field distribution calculated from FDTD.

2.5 Conclusion

In this Chapter, Hamiltonian ray tracing method has been introduced and its extension to complex media such as photonic crystals and metamaterials has been addressed. Traditional Hamiltonian equations are based on screen Hamiltonian or 3D Hamiltonian. For easy wavefronts generation and physical insights, 3D OPL Hamiltonian ray tracing is derived and applied to Lüneburg lens. Hamilton equations for photonic crystals are presented and it has been proven that they are equivalent to conventional Hamiltonian equations. Hamiltonian optics provide a faster solution to the beam propagation analysis of photonic crystals comparing with FDTD method. Hamiltonian equations can also be applied to metamaterials by incorporating effective medium theory. Aperiodic subwavelength nanostructured Lüneburg lenses, both in 2D and in 3D, are designed and verified as examples of this method.

Chapter 3

Hamiltonian ray tracing for wave propagation

Optical wave propagation in inhomogeneous materials has become an important problem in research fields such as photonic crystals [66] and metamaterials [28]. Conventional treatment to this problem, the finite-difference time-domain (FDTD) method, can simulate wave propagation in an inhomogeneous medium, but it is computationally complex and physically less intuitive than ray diagrams. Therefore, up to now, a lot of work has been done to employ the ray-tracing methods, such as Hamiltonian ray-tracing, to analyze beam propagation in these materials. However, ray tracing, as have been discussed in Chapter 2, is based on geometrical optics and thus does not take the wave optics phenomena into account. Researchers keep on finding a ray-tracing extension to account for wave optics effects. For example, Keller introduced a theory of geometrical diffraction [51] and had extended it to inhomogeneous media [34].

In this Chapter, we propose an alternate method [36], which has more physical foundation, for simulation of wave optics effects in an inhomogeneous medium. Our method uses the Wigner distribution function (WDF) as initial condition required for Hamiltonian ray-tracing. We first start with a brief introduction of the WDF, with its physical meanings and properties. Then the method is presented and the general procedures are highlighted. A Gaussian beam propagation in free space is taken as

an example. Beside, as examples to validate the approach, we have simulated the propagation of a Gaussian beam through an elliptical GRIN medium, and Lagurre-Gaussian rotating beam propagation. At the very beginning, let us start with the basics of the WDF.

3.1 Introduction to the Wigner distribution function

The Wigner distribution function was introduced by E. Wigner in quantum mechanics in 1932 [105]. Later, it has been applied to optics by A. Walther [103]. It is a mathematical tool for representing signals in phase space. It could simultaneously provide information about the spatial properties and angular spectrum of a signal.

The WDF of a coherent optical signal $f(x)$ is defined by

$$\mathcal{W}(x, u) = \int f\left(x + \frac{x'}{2}\right) f^*\left(x - \frac{x'}{2}\right) \exp(-i2\pi ux') dx', \quad (3.1)$$

where x is the position and u is the spatial frequency.

Also, if given a coherent optical signal with Fourier transform $F(u)$, the WDF is defined similarly by

$$\mathcal{W}(x, u) = \int F\left(u + \frac{u'}{2}\right) F^*\left(u - \frac{u'}{2}\right) \exp(i2\pi xu') du'. \quad (3.2)$$

The WDF, as applied to optics, defined the generalized radiance for certain position and momentum [103, 106]. It has many interesting properties. Some of them which are utilized in the thesis are listed below:

1. Realness. The WDF is always real:

$$\mathcal{W}(x, u) = \mathcal{W}^*(x, u). \quad (3.3)$$

This property is consistent with the physical meaning of WDF since generalized radiance should not have imaginary part.

2. Region property. If $f(x) = 0$ for $x < x_0$, $\mathcal{W}(x, u) = 0$ for $x < x_0$, or vice versa.

3. Projection property. Energy related quantities can be expressed as projections of the WDF.

- *Intensity:* A projection along momentum u direction.

$$I(x) = |f(x)|^2 = \int \mathcal{W}(x, u) du. \quad (3.4)$$

- *Fourier spectrum intensity:* A projection along position x direction.

$$I_u(u) = |F(u)|^2 = \int \mathcal{W}(x, u) dx. \quad (3.5)$$

- *Total energy:* a 2D integral on the WDF plane.

$$E = \int |f(x)|^2 dx = \int |F(u)|^2 du = \iint \mathcal{W}(x, u) dx du. \quad (3.6)$$

It is also helpful to start with the WDF of some special optical signals listed below:

1. Point source. Assuming that a point source is located at position x_0 , the signal is expressed as $f(x) = \delta(x - x_0)$. The WDF takes the form:

$$\mathcal{W}(x, u) = \delta(x - x_0), \quad (3.7)$$

which is a vertical line along the u direction at position x_0 .

2. Plane wave. Assuming that a plane wave is with spatial frequency u_0 (related to the direction of propagation), the signal is expressed as $f(x) = \exp(i2\pi u_0 x)$. The WDF takes the form:

$$\mathcal{W}(x, u) = \delta(u - u_0), \quad (3.8)$$

which is a horizontal line along the x direction at spatial frequency u_0 .

3. Gaussian beam. Assuming that we have a Gaussian beam $f(x) = \exp(-\frac{\pi}{\sigma^2}(x -$

$x_0)^2$), its WDF can be written as:

$$\mathcal{W}(x, u) = \exp \left\{ \left(\frac{2\pi}{\sigma^2} (x - x_0)^2 + \frac{\sigma^2}{2\pi} u^2 \right) \right\}, \quad (3.9)$$

which is Gaussian distribution in both x and u directions.

3.2 Wave propagation examples

Ray tracing method, such as Hamiltonian ray tracing, is computationally more efficient and provides more physical insights into the radiance evolution for the beam propagation. However, ray tracing is based on geometric optics so that wave effects are lost during propagation. It will be very useful if wave phenomena could be included in ray tracing. In this section, we show that wave effect can be considered in ray tracing by defining the initial condition of rays with the WDF. Several examples are implemented to validate this method.

The WDF provides a connection between rays and waves [98]. The local spatial frequency (or momentum in Hamiltonian ray tracing language) corresponds to the angle of a ray in geometric optics [43]. Huygens' principle states that for each point of a wavefront, it has multiple rays emitting out. Each ray has different position and momentum, and carries the generalized radiance defined by the WDF [103, 106, 98]. Therefore, each ray corresponds to one point as the WDF plane, with position, momentum and generalized radiance defined (Fig. 3-1). Bastiaans has proven that the value of WDF, i.e. the generalized radiance, keeps constant along the ray [9, 10].

From the discussions above, for this method combining the Hamiltonian ray tracing and the WDF, three key points are worth emphasizing:

1. Each point on the WDF plane can be treated as a ray;
2. Ray path in the medium is governed by the Hamiltonian ray tracing equations;
3. The generalized radiance carried by each ray, as defined by the value of WDF, keeps constant along the ray path.

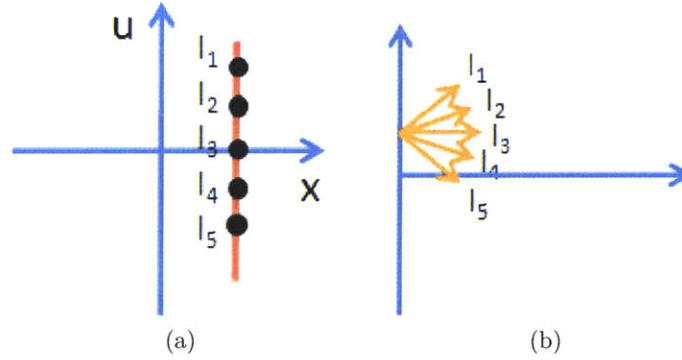


Figure 3-1: Relationship between the WDF and initial condition of rays defined. Each ray corresponds to one single point on the WDF plane. (a) The WDF plane with five points chosen at the same position but different momenta. (b) Five rays emitting from the same position defined through the five points on the WDF plane. The directions of them are related to the momenta in (a) and generalized radiances are proportional to the values of WDF.

With the ray tracing results on hand, the optical intensity at certain position can be calculated by summing up the generalized radiances carried by all the rays passing through this point. This is equivalent to perform a projection along u direction on the WDF plane.

In this way, the diffraction has been taken into account by simply using Hamiltonian ray tracing with initial conditions defined by the WDF.

3.2.1 Single and double-slit diffraction

As the first example, the fundamental wave effects, the single and double-slit diffraction, are performed to validate the method proposed in this Chapter.

For the two cases, the WDF of the input, either single slit or double slit, is calculated. Then for each point on the WDF plane, one ray is defined accordingly. For each ray, Hamiltonian ray tracing equations are solved to find the final position of this ray at the output plane. Since currently the medium is free space so the Hamiltonian ray tracing is not used in practice but rays are simply straight lines. Finally, the intensity distribution of the output plane is generated by a projection on the WDF plane.

The results are shown in Fig. 3-2. Here the free space wavelength is chosen as $\lambda = 1$ mm and propagation length $L = 1000$ m. For the single-slit case, the slit width is $w = 0.1$ m. The WDF and the calculated diffraction pattern at the output plane are illustrated. From the intensity pattern, the distance between two neighboring intensity minimum points is 10 m, which matches the result from analytical solution:

$$\Delta x = \frac{\lambda L}{w} = 10 \text{ m.} \quad (3.10)$$

Also, for the double-slit case, the slit width is again $w = 0.1$ m and the distance between the two slit centers is $d = 0.4$ m. The WDF shows that besides the patterns of the two slits, there is another pattern with some negative generalized radiances in between. This is the interference pattern of the WDF and it contributes to the interaction between the two slits, namely interference. From the intensity pattern, the distance between two neighboring intensity maximum points is 2.5 m, which matches the result from analytical solution:

$$\Delta x = \frac{\lambda L}{d} = 2.5 \text{ m.} \quad (3.11)$$

From all the discussions above, this method is able to include the wave effects by simply using geometric ray tracing.

3.2.2 Gaussian beams in free space

In this subsection, a Gaussian beam is generated with the method discussed in previous section and verified with analytical results in free space. For a 2D Gaussian beam, the intensity distribution is

$$I(x, z) = I_0 \left(\frac{w_0}{w(z)} \right) \exp \left(\frac{-2x^2}{w^2(z)} \right), \quad (3.12)$$

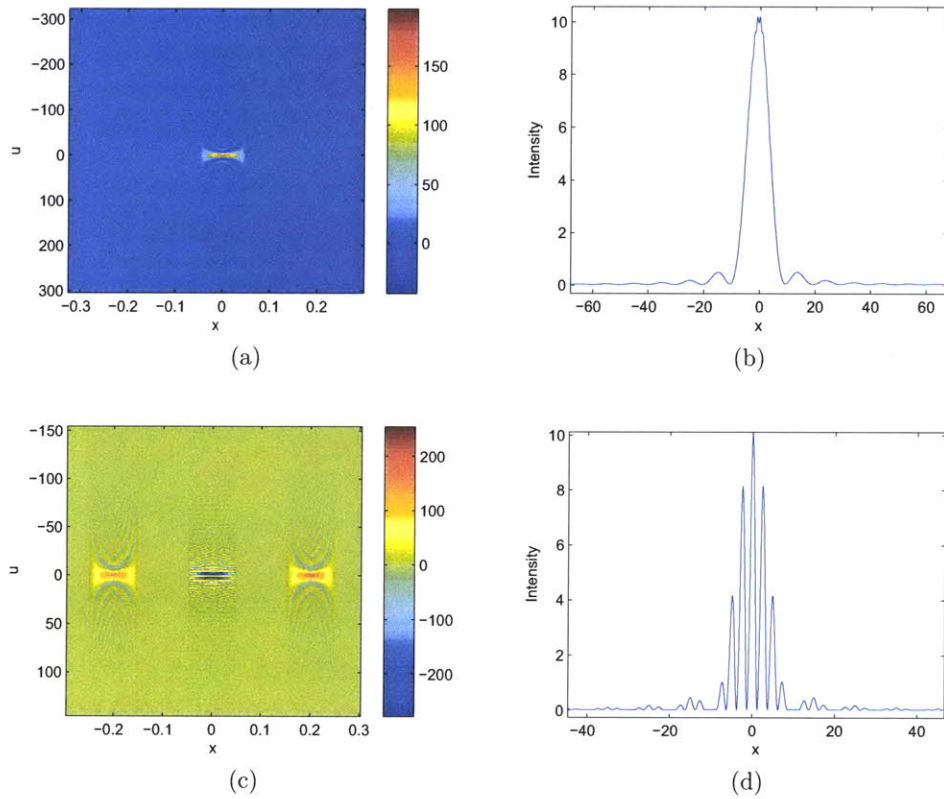


Figure 3-2: Single and double-slit diffraction results calculated based on the method discussed in this Chapter. (a) The WDF of the single-slit. (b) The diffraction pattern of the single-slit at the output plane. (c) The WDF of the double-slit. (d) The diffraction pattern of the double-slit at the output plane.

where

$$w(z) = w_0 \sqrt{1 + \left(\frac{z}{z_R}\right)^2}, \quad z_R = \frac{\pi w_0^2}{\lambda}. \quad (3.13)$$

For the case used in the simulation, the Gaussian beam illumination at the initial input plane is chosen as:

$$E(x, z) = E_0 \exp\left(-\frac{x^2}{2\sigma^2}\right), \quad (3.14)$$

where $E_0 = 1$ and $\sigma = 0.02$ m. Note that in this Chapter, Gaussian beams are assumed to be two dimensional, meaning that there is only one transversal axis x . The electric field profile as well as its WDF are illustrated in Fig. 3-3.

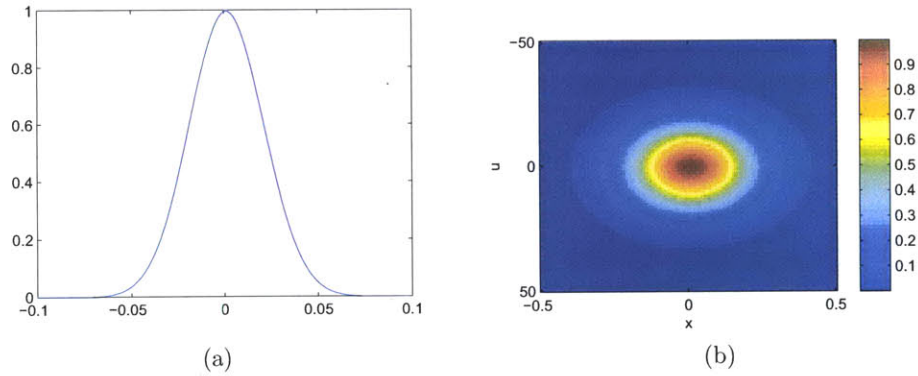


Figure 3-3: Electric field distribution (a) and the WDF (b) for the input Gaussian source.

Based on the WDF defined initial condition for rays, the Gaussian beam profile propagating in free space can be generated as is shown in Fig. 3-4. In order to validate this method, it is important to make a comparison of the generated beam profile with that given by analytical results. To meet this goal, curve fitting is implemented to make such a comparison.

First, for every z plane on the z axis, the intensity is obtained and curve-fitted with the analytical expression of a Gaussian distribution since every z axis should be a normal distribution for a Gaussian beam propagation. We include 2001 z planes

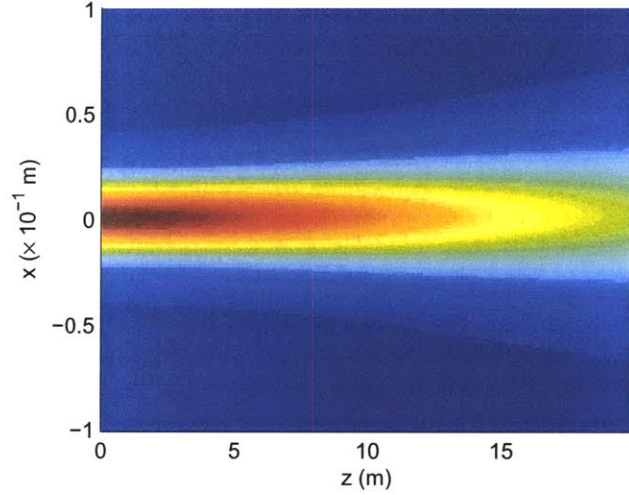


Figure 3-4: Gaussian beam profile while propagating in free space

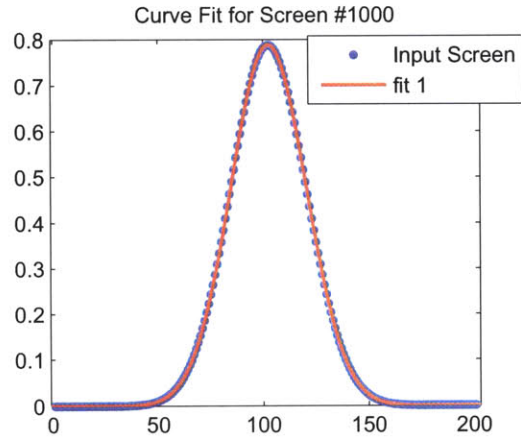
from $z = 0$ m to $z = 20$ m with an interval of 0.1 m. The analytical formula used for curve fitting is $a_1 \cdot \exp(-((x - b_1)/c_1)^2)$.

Curve fitting results are shown in Fig. 3-5. From goodness of fit results, it can be seen that every z plane keeps a very good Gaussian distribution. The sum squared error (SSE) and root mean square error (RMSE) are almost zero. The coefficient of determination (R^2) and degree-of-freedom adjusted coefficient of determination (adjusted R^2) are almost one. The evolution of a_1 and c_1 for curve fitting at different z planes is also shown below in Fig. 3-6. A very good agreement can be seen between curve-fitting data and analytical results. Therefore, the method discussed in this Chapter provides a valid solution to the Gaussian beam propagation in free space.

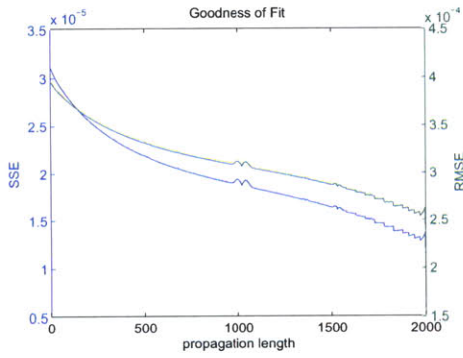
3.2.3 Gaussian beams in elliptical GRIN medium

In this subsection, propagation of a Gaussian beam in elliptical GRIN medium is investigated as another example. The illuminating Gaussian source is shown in Fig. 3-7(a). The elliptical GRIN medium has a refractive index distribution of $n(x) = \sqrt{n_0^2 - \kappa^2 x^2}$ where $n_0 = 1.5$ and $\kappa = 0.45 \text{ m}^{-1}$, as shown in Fig. 3-7(b). It is invariant along z direction and changes only in the transverse x direction.

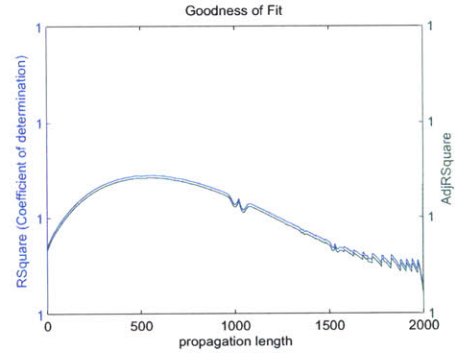
The results are shown in Fig. 3-7(c)(d). Sampled ray tracing results clearly show



(a)



(b)



(c)

Figure 3-5: Curve fitting results for Gaussian beam propagation in free space. (a) One example of curve fitting at $z = 10$ m. Blue dots are the original intensity data and red curve is the curve fitting result. (b) Parameters for the goodness of fit at different z planes: SSE and RMSE. (c) Parameters for the goodness of fit at different z planes: R^2 and adjusted R^2

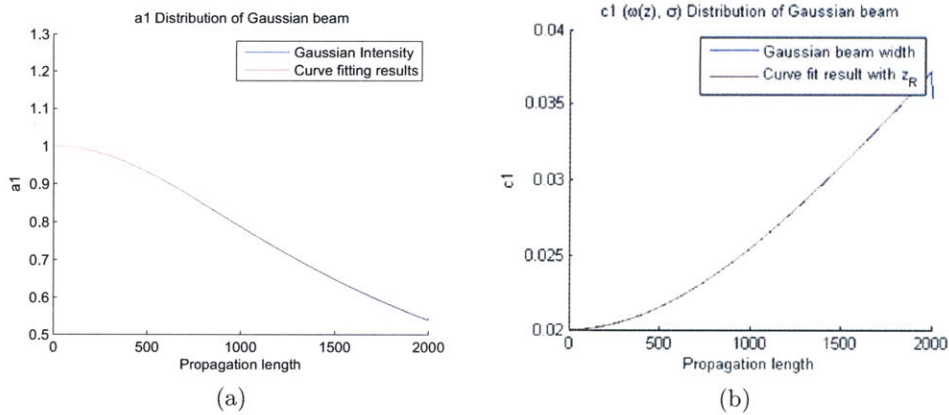


Figure 3-6: Curve fitting results for Gaussian beam propagation in free space. (a) a_1 distribution along different z planes. Blue line is the analytical result and red line is the curve-fitting result. (b) c_1 distribution along different z planes. Blue line is the analytical result and red line is the curve-fitting result.

the periodic focusing of rays in the region under investigation. This matches the intensity profile where periodic focusing can be located at the same spots as ray tracing. Diffraction has been taken into account since one initial point has multiple rays emitting and some of them focus away from the center.

3.2.4 Rotating beams

Rotating beam [89, 83] is an intensity distribution which gradually and continuously rotates with respect to its optical axis as it propagates. This property has attracted much research attention and a lot of works have been done on rotating beams, including highly efficient rotating PSFs [75], fluorescence imaging beyond the diffraction limit [76] and optical manipulation of particles [4].

Rotating beam can be achieved through a combination of different Laguerre-Gaussian (LG) modes. LG mode is written as [83]

$$u_{n,m}(\mathbf{r}) = C_{n,m}G(\rho, z)R_{n,m}(\rho/w(z))\Phi_m(\varphi)Z_n(z). \quad (3.15)$$

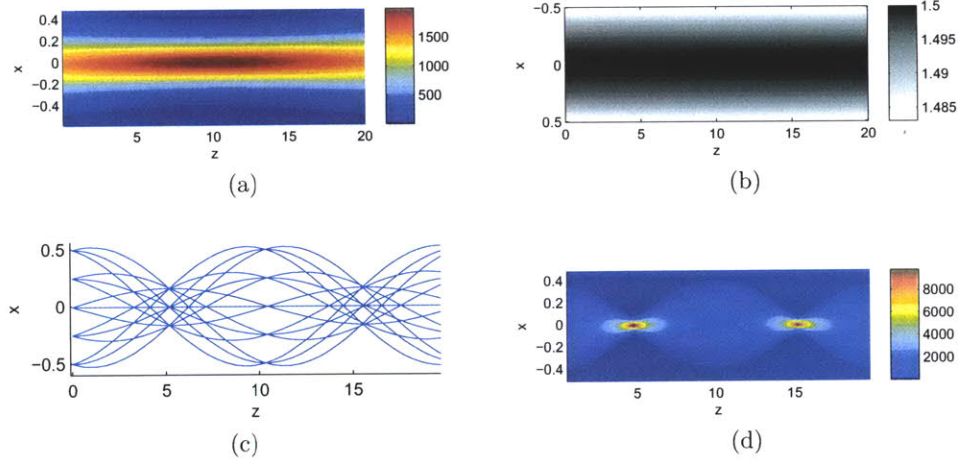


Figure 3-7: Gaussian beam propagation in elliptical GRIN medium. (a) The input Gaussian beam in free space. (b) Refractive index profile of the elliptical GRIN medium. (c) Sampled rays from ray tracing results for Gaussian beam propagation. (d) Beam propagation results in this elliptical medium.

The terms on the right-hand side are

$$C_{n,m} = \left[\left(\frac{n - |m|}{2} \right)! |m|! \right] / \left[\sqrt{2}^{|m|} \left(\frac{n + |m|}{2} \right)! \right]; \quad (3.16)$$

$$G(\rho, z) = \frac{w_0}{w(z)} \exp \left[-\frac{\rho^2}{w(z)^2} \right] \exp \left[\frac{ik\rho^2}{2w(z)^2 R(z)} \right] \exp \left[-i \arctan \left(\frac{z}{z_0} \right) \right], \quad (3.17)$$

where $w(z) = w_0[1 + (z/z_0)^2]^{1/2}$ is the Gaussian spot size, $z_0 = \pi w_0^2/\lambda$ is the Rayleigh length, $\arctan(z/z_0)$ is the Gouy phase, and $R(z) = z[1 + (z_0/z)^2]$ is the radius of curvature of the wavefront;

$$R_{n,m}(\rho/w(z)) = \left[\frac{\sqrt{2}\rho}{w(z)} \right]^{|m|} L_{(n-|m|)/2}^{|m|} \left[\frac{2\rho^2}{w(z)^2} \right]; \quad (3.18)$$

where $L_{(n-|m|)/2}^{|m|}$ are the generalized Laguerre polynomials with integers n and m following $n = |m|, |m| + 2, |m| + 4, \dots$;

$$\Phi_m(\varphi) = \exp[im\varphi]; \quad (3.19)$$

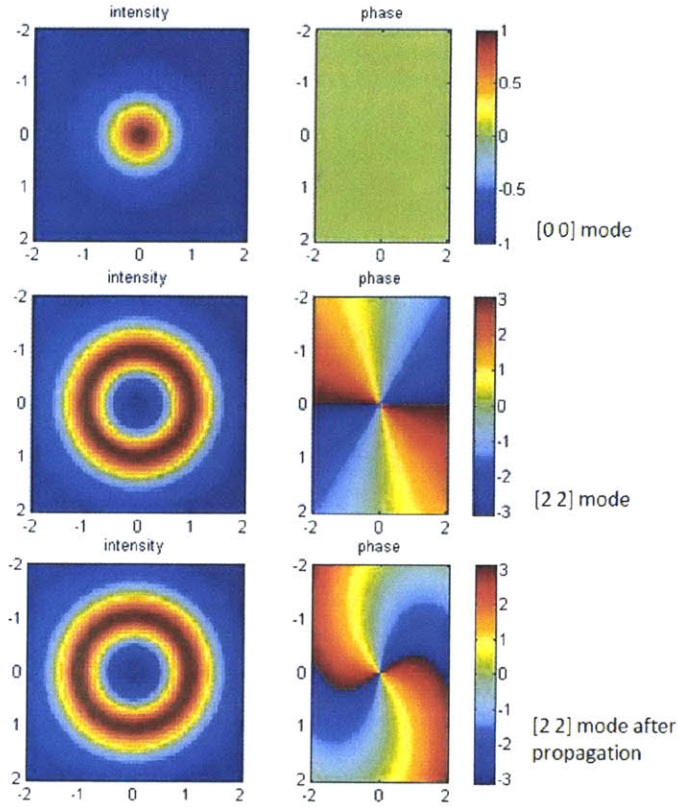


Figure 3-8: Intensity and phase profiles for typical Laguerre-Gaussian modes. (0 0) and (2 2) modes are illustrated as well as (2 2) mode after propagation. Left column contains intensity profiles while right column contains phase profiles.

$$Z_n(z) = \exp \left[-in \arctan \left(\frac{z}{z_0} \right) \right]. \quad (3.20)$$

The intensity and phase profiles for typical Laguerre-Gaussian modes ((0 0) and (2 2) modes) are illustrated in Fig. 3-8. From the figure we see that (0 0) mode is normal Gaussian profile with constant phase. However, for (2 2) mode which is high-order mode, intensity profile becomes donut-shaped and the phase changes by 2π when rotating by 180 degrees. The intensity profile of (2 2) mode after some propagation is also illustrated in Fig. 3-8, from which it can be observed that the intensity keeps invariant while the phase is twisted around the center.

While combining different LG modes together, the beam profile is a result of interference among different modes. As a result, the final beam profile rotates as the

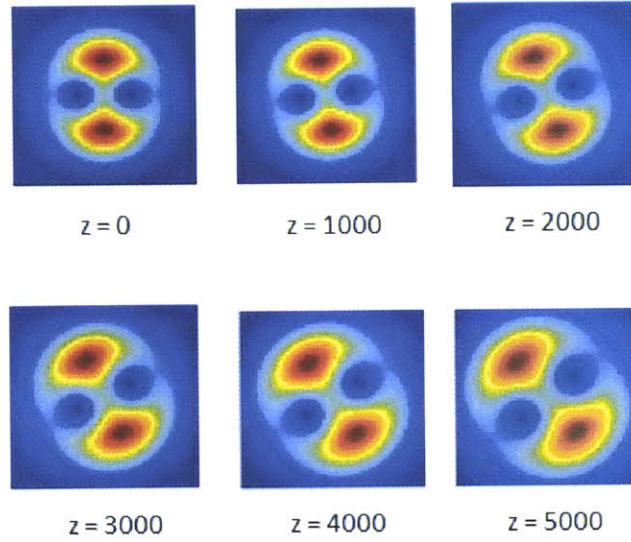


Figure 3-9: The intensity profiles of rotating beam at different propagation lengths. A superposition of (0 0) and (2 2) LG modes is used as the illumination. The unit for z is meter.

beam propagates. Rotating beam is a superposition of different LG modes. Assuming free space illuminated by a superposition of (0 0) and (2 2) modes, the beam intensity profiles at different propagation lengths are calculated based on the analytical results in Eq. 3.15. The results are shown in Fig. 3-9. In this case, for convenience, free space wavelength is chosen as $\lambda = 500 \mu\text{m}$ and $w_0 = 1 \text{ m}$.

It is interesting to investigate the reason for the rotation of beam from the WDF perspective. The WDF of LG mode is obtained through either analytical derivation [89] or numerical evaluation of the definition of WDF applied to LG mode. Since for the LG mode discussed in this section, it is 2D so that the WDF of it is 4D. It is difficult to plot 4D WDF so a compromise has been made to illustrate the WDF as in Fig. 3-10. The middle figure is the projection on the (x, y) plane so it is the intensity profile. By investigating the (u, v) profiles at four different positions of the mode, it can be seen that the positions of positive generalized radiances are always at the rotating direction of that specific point, and vice versa. Since (u, v) is an indication of ray directions, the beam is rotating based on the WDF picture.

The rotating beam is investigated with the method discussed in this Chapter, with

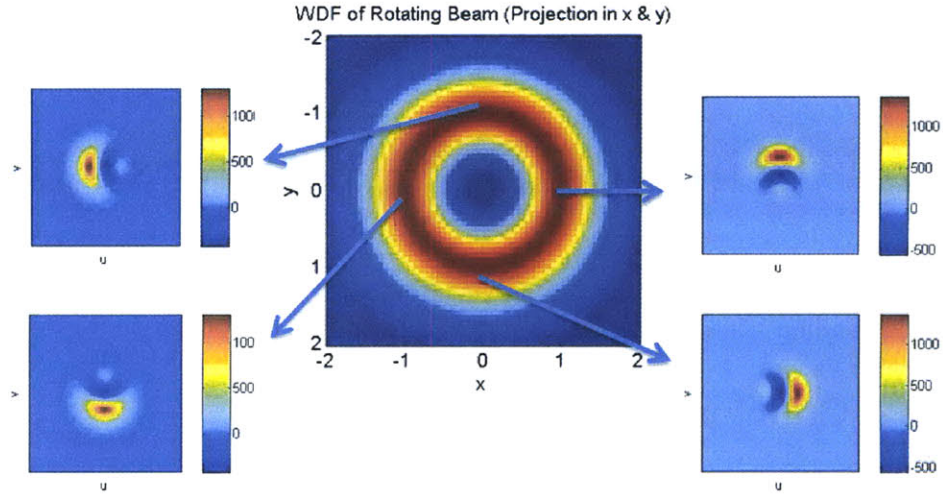


Figure 3-10: The WDF of (2 2) mode. The middle figure shows the WDF with a projection of (u, v) on the (x, y) plane. Four small figures illustrated the (u, v) distribution for a specific (x, y) . Here (x, y) is certain position and u, v are the spatial frequencies (ray directions) along x and y directions, respectively.

the same parameter as in Fig. 3-9. The illumination is again a combination of (0 0) and (2 2) modes. According to the results shown in Fig. 3-11, beam rotation can be clearly seen. Some artifacts occur along the edge of the beam profile, which is due to the low resolution of WDF used limited by the computer memory.

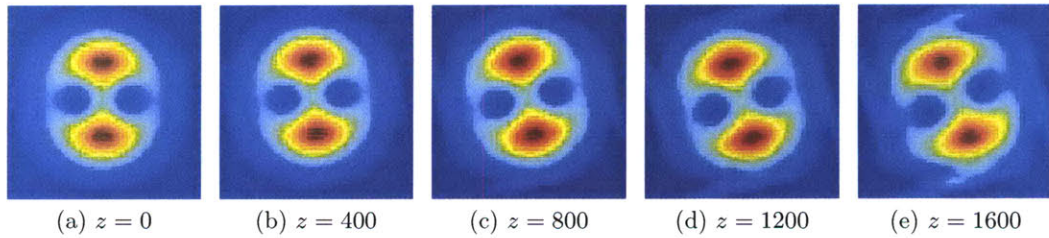


Figure 3-11: Rotating beam profile evolution as the beam propagates based on the method discussed in this Chapter.

In addition, the rotating beam is also analyzed in the elliptical GRIN medium with refractive index distribution $n(x, y) = \sqrt{n_0^2 - \kappa^2(x^2 + y^2)}$. Based on the results shown in Fig. 3-12, the beam rotates as it propagates, while at the same time, the beam size oscillates as a result of the GRIN medium.

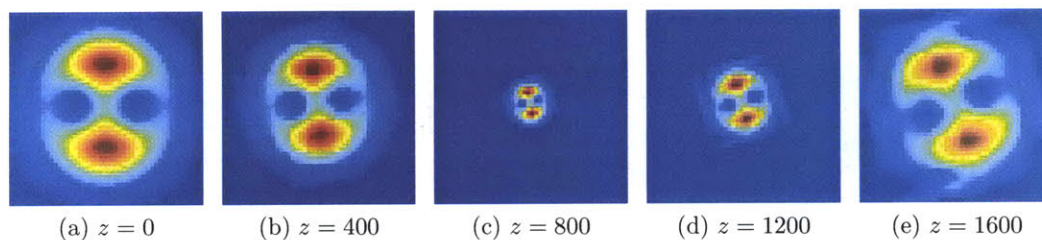


Figure 3-12: Rotating beam profile evolution as the beam propagates in elliptical GRIN medium based on the method discussed in this Chapter.

3.3 Conclusion

In this Chapter, a method for including wave effects into ray tracing has been introduced by defining the initial conditions of Hamiltonian ray tracing using the WDF. This method is physically intuitive and offers more physical insights into the generalized radiance evolution in certain media. Examples are given to validate this method, including single and double-slit diffraction, Gaussian beam propagation in free space and elliptical GRIN medium, and rotating beam propagation in these media. In addition, this method is also useful in nonlinear media. Nonlinear media are very important in many cases and beam propagation in nonlinear optical media should be very beneficial. In the following chapter, the method presented here will be extended to the iterative nonlinear beam propagation method. It will not only solve the nonlinear beam propagation problem but also preserves the intuitive ray tracing perspective.

Chapter 4

Iterative nonlinear beam propagation method

Nonlinear beam propagation plays a very important role in investigation of nonlinear optical devices and systems, such as integrated optical systems [47], optical fiber communication systems [2], etc. With the development of research on photonic crystals and metamaterials, their properties with nonlinearity have been investigated [26, 17]. Many methods for nonlinear beam propagation have been introduced in literature. Three categories of typical methods are briefly presented as follows.

(1) Split-step beam propagation method (BPM). BPM [2, 99, 90] is a conventional treatment of nonlinear beam propagation, providing a step-wise solution of nonlinear Schrödinger (NLS) equation in coherent regime. The NLS equation is written as [54]

$$\nabla^2 \mathbf{E} - \frac{1}{c^2} \frac{\partial^2 \mathbf{E}}{\partial t^2} = \frac{1}{\epsilon_0 c^2} \frac{\partial^2 \mathbf{P}}{\partial t^2}, \quad (4.1)$$

where \mathbf{E} is the electric field, \mathbf{P} is the induced polarization, c is the speed of light and ϵ_0 is the permittivity in vacuum. Assuming that the beam is propagating along z direction (optical axis), electrical field could be expresses as $E(\mathbf{r}, t) = A(\mathbf{r}) \exp(ik_0 n_0 z)$, where A is certain amplitude, n_0 and k_0 are refractive index and wavenumber in vacuum. Under paraxial approximation, in nonlinear Kerr effect medium, NLS equation

becomes

$$2in_0k_0\frac{\partial A}{\partial z} + \left(\frac{\partial^2 A}{\partial x^2} + \frac{\partial^2 A}{\partial y^2}\right) + 2k_0^2n_0n_2IA = 0. \quad (4.2)$$

where n_2 is Kerr effect coefficient and I is optical intensity. Thus the evolution of optical field along z direction is governed by two factors: the diffraction term (second term of Eq. (4.2)) and the nonlinear term (third term of Eq. (4.2)). BPM solves the beam propagation solution step by step along z direction. For each smaller enough z step Δz , BPM assumes that effects due to diffraction and nonlinearity can be treated as independent. Therefore, optical fields on the two neighboring z slides are related by [78]

$$\mathbf{E}(x, y, z + \Delta z) = \exp(-ik_0n_2I)\mathcal{F}^{-1}\left\{\exp\left[\frac{i(k_x^2 + k_y^2)\Delta z}{2k_0}\right]\mathcal{F}\{\mathbf{E}(x, y, z)\}\right\}. \quad (4.3)$$

In each calculation step, BPM takes the current optical field, performs Fourier transform and adds the diffraction term $\exp[i(k_x^2 + k_y^2)\Delta z/(2k_0)]$, which is the transfer function for beam propagation in linear media. Then it performs the inverse Fourier transform and adds the nonlinear term $\exp(-ik_0n_2I)$ in the space domain. The whole beam propagation profile can be generated based on the step-wise solution.

(2) Partially coherent regime methods. With the discovery of partially coherent solitons [67], several methods aiming at nonlinear beam propagation in partially coherent regime have been presented. Among them, one method is based on the propagation of mutual coherence function and accounts for refraction [86]. In self-consistent multimode theory [68], the incoherent beam is treated as a multimode waveguide which in turn guides the beam itself. Analysis of this multimode waveguide is carried out by multiply populating the guided modes. For coherent density method [23], an infinite set of coupled nonlinear Schrödinger-like equations are provided from incoherent angular spectrum of the illumination. Later, Christodoulides *et al.* have proved that these methods are equivalent [24].

(3) Wigner distribution function approaches. It is physically intuitive if ray di-

agrams are generated in the nonlinear beam propagation investigation. With ray diagrams, radiance evolution for the beam propagation profile is obvious. In order to achieve this goal, methods based on the Wigner distribution functions (WDF) have been introduced [29, 45]. These methods derive a set of differential equations governing the transport of radiance. However, due to the coupling between optical intensity and refractive index, solving these equations is not straight forward.

In this Chapter, an iterative nonlinear beam propagation method [39] is proposed to provide ray diagrams which are physically more intuitive. At the same time, wave effects and coherent properties are preserved, meaning that this method not only takes the wave effects, such as diffraction and interferences into account, but also works in both coherent and partially coherent regime. With Kerr nonlinearity, this iterative method is verified in coherent regime with self-focusing and spatial solitons, and is also validated by Gaussian-Schell model propagation in partially coherent regime. This iterative nonlinear beam propagation method provides a recipe for the investigation of nonlinear metamaterials and devices. In the next Chapter, a nonlinear Lüneburg lens is taken as example for this application.

4.1 Iterative nonlinear beam propagation method

The proposed iterative nonlinear beam propagation method is based on Hamiltonian ray tracing [107] and the WDF [103, 106, 11, 5]. Throughout this Chapter, without loss of generality, bulk media with Kerr effect nonlinearity [16] are used to demonstrate the method. The common phenomenological Kerr index dependence on the optical intensity as $n = n_0 + n_2 I$ is used, where n_0 is the linear component of the refractive index, n_2 is the Kerr coefficient and I is the optical intensity.

The block diagram of the method is shown in Fig. 4-1.

The method consists of three steps in one iteration: (1) Define the initial condition for each ray emanating from the input plane; the value of the radiance of each ray is computed from the WDF of the input field; (2) Solve the Hamiltonian ray tracing equations for each ray; (3) Generate the intensity distribution and update the

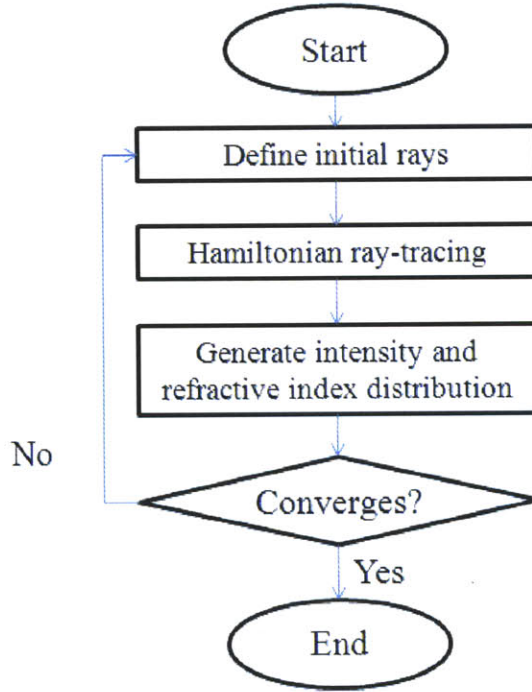


Figure 4-1: Block diagram of the iterative nonlinear beam propagation method.

refractive index distribution.

In the first step, the initial position and momentum of the rays for the input illumination are defined based on the WDF, which is used as the initial condition for Hamiltonian ray tracing in Step 2. The WDF [11, 5] defines the generalized radiance of every position and momentum. Thus every discretized point on the WDF plane corresponds to one ray, with the corresponding position and momentum defined. The generalized radiance carried by the ray is defined by the value of WDF of the corresponding point. Generalized radiance, as compared with classical radiance, includes wave effects into ray tracing [5]. Therefore, each input position has multiple rays emanating with different momenta, which is suggested by Huygens' principle; and wave effects are taken into account through this consideration.

To better illustrate this point, a Gaussian beam propagation in free space is presented in Fig. 4-2. Fig. 4-2(a) shows the WDF of a Gaussian source computed at the initial plane in one dimension, and Fig. 4-2(b) illustrates the Gaussian intensity profile along the propagation direction. This is generated by solving the Hamiltonian

equations for each ray with the initial condition defined by the WDF in Fig. 4-2(a). The intensity profile matches well with the analytical solutions of Gaussian beam in two dimension. Reader may want to refer to Chapter 3 for a detailed discussion on Hamiltonian ray tracing applied to wave propagation using the WDF.

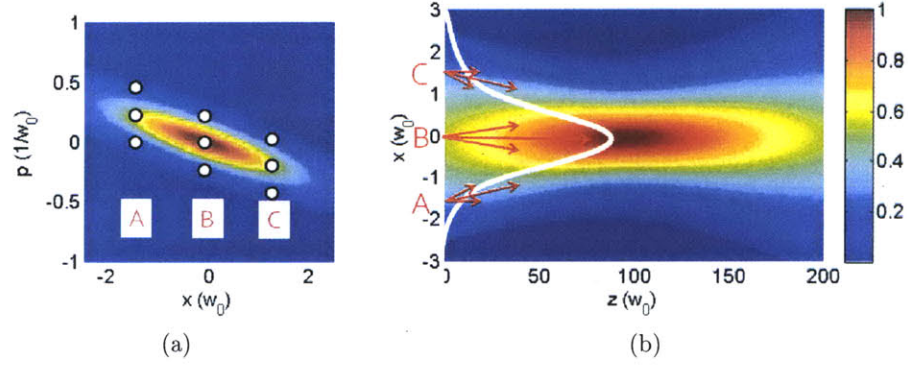


Figure 4-2: The WDF of the Gaussian beam at the input plane in one dimension (a), and Gaussian beam generated from rays with initial condition specified by the WDF (b). Here x is position and p is momentum. All numbers are scaled according to the waist w_0 . Free space wavelength is $\lambda = w_0/20$. Nine points on the WDF plane (white dots in (a)) correspond to 9 rays (arrows in (b)). Three different ray directions are shown for each of the 3 positions (A-C). The lengths of arrows are proportional to the generalized radiance of the WDF.

What is more, the WDF can also describe partially coherent light [12]. Thus this method is also applicable for simulation of the beam propagation in partially coherent regime.

In the second step, Hamiltonian ray tracing is applied to each of the ray defined in the previous step. Hamiltonian ray tracing solves the two differential equations governing the ray trajectories [107]:

$$\frac{d\mathbf{q}}{d\sigma} = \frac{\partial H}{\partial \mathbf{p}} = \frac{\mathbf{p}}{|\mathbf{p}|}, \quad \frac{d\mathbf{p}}{d\sigma} = -\frac{\partial H}{\partial \mathbf{q}} = \frac{\partial n}{\partial \mathbf{q}}, \quad (4.4)$$

where \mathbf{q} and \mathbf{p} are position and momentum along the path, $H = |\mathbf{p}| - n$ is the 3D Hamiltonian, n is the refractive index and σ parameterizes the ray trajectories. Hamiltonian ray tracing is computationally efficient than the FDTD method. Detailed discussions on Hamiltonian ray tracing can be found at previous chapters.

In the third step, the optical intensity of each point of the nonlinear media is calculated through the projection in the momentum direction on the WDF of the corresponding plane, which is generated based on the Hamiltonian ray tracing results. This is shown in Fig. 4-3. Also, an updated refractive index is calculated based on the intensity through the Kerr effect relationship, where refractive index changes linearly to the optical intensity.

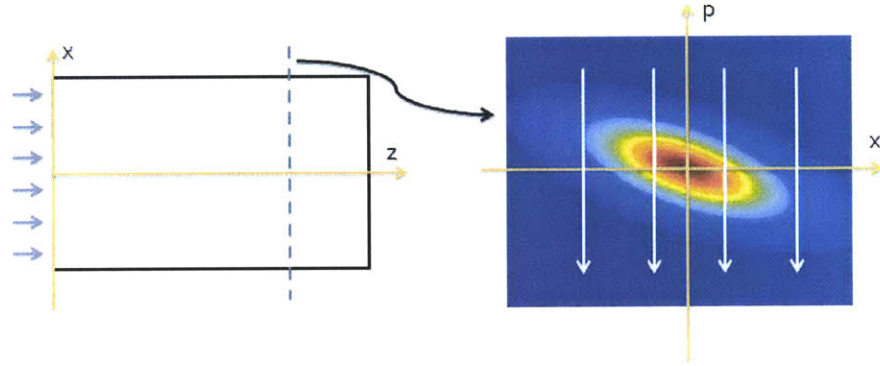


Figure 4-3: Optical intensity generation based on the Hamiltonian ray tracing results. Here x is position, z is optical axis and p is momentum. Blue dashed line is the calculating plane and color shading is the WDF generated from all the rays (with different positions and momenta) passing through this plane. Intensity distribution along this plane is calculated through a projection along the momentum direction (white arrows) on the WDF.

After one iteration, ray tracing is again applied to the new refractive index profile and another updated version of refractive index is generated. Finally the iterations converge and the final intensity profile is the beam propagation results we seek. The convergence condition is:

$$\sum_{All\ points} |I_{current} - I_{pre}| < \epsilon \quad (4.5)$$

where the difference between the intensities generated at two consecutive iterations is expected to be below certain threshold.

This method provides a ray picture to the nonlinear beam propagation which is physically more intuitive, offering an insight into the radiance evolution in the non-

linear media. Also, it has the potential application in optical system design softwares such as ZEMAX, where ray tracing is generally used. With this iterative method, while dealing with nonlinear element, it could be consistent with the ray tracing throughout the analysis, avoiding the transition between rays and waves. Furthermore, it has been proved that Hamiltonian ray tracing, under the locally periodic assumption, is valid in photonic nanostructures [49, 81]. Thus, this iterative method could also be applied to nonlinear metamaterials and nanophotonics devices, providing a systematic approach to nonlinear beam propagation simulation in these devices. An example, nonlinear subwavelength nanostructured Lüneburg lens, is investigated in the next chapter.

4.2 Examples

The proposed iterative nonlinear beam propagation method is validated with self-focusing [22, 52] and spatial soliton [54] phenomena in nonlinear Kerr effect media with totally coherent illumination. In the partially coherent regime, Gaussian-Schell model is investigated and the results agree with those provided in [96].

4.2.1 Self-focusing

Self-focusing is a well known phenomena [22, 52]. It results from the competition between diffraction and nonlinearity. Diffraction expands the light beam while Kerr nonlinearity creates a waveguide by itself and focuses the beam. In the case that the focusing effect due to nonlinearity is stronger than the expansion effect due to the diffraction, self-focusing happens. In a bulk Kerr effect medium with Gaussian beam input, multiple foci occur in periodically spaced locations along the optical axis, as a result of the interaction between the diffraction and the nonlinearity [16].

The first example is taken as the periodic self-focusing of a Gaussian beam in a weak Kerr effect medium. In this example, the original linear refractive index of medium is $n_0 = 1.5$ and Kerr effect coefficient is $n_2 = 2 \times 10^{-13} \text{ (m/V)}^2$. The input Gaussian beam has a waist of 2 mm and a peak amplitude of 250 V/m, which is

equivalent to intensity of 12.4 mW/cm^2 . Length of propagation is 100 m. After 11 iterations, the intensity distribution estimates converge. Fig. 4-4(a) shows the converged beam propagation results. As a comparison, the result produced by BPM is shown in Fig. 4-4(b). They match well. Computation time for iterative method is 2.1 minutes while for BPM it is 33 seconds.

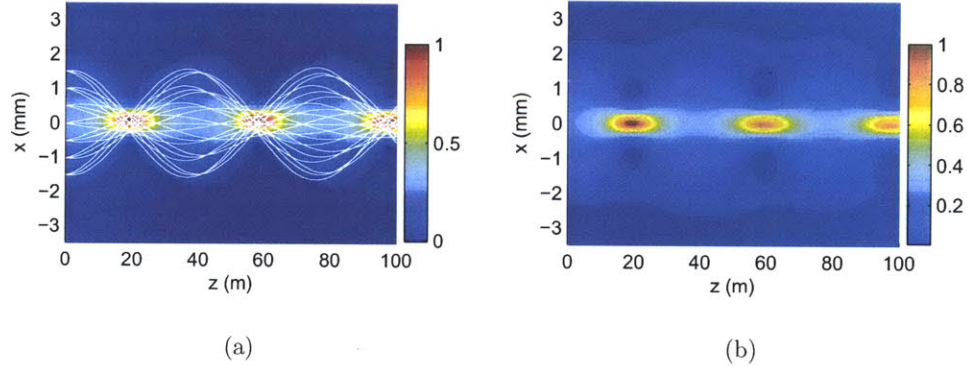


Figure 4-4: Periodic self-focusing of Gaussian beam in Kerr medium produced by the iterative method (a) and BPM (b). The white lines are a subset of all 10100 rays used in the simulation. The color shading represents intensity, computed as projection along the momentum direction from the generated WDF.

For the second example a change of source is made from a single Gaussian beam into two identical Gaussian beams located at different positions of the input plane. They are parallel to each other and propagating into the Kerr effect medium. The same medium is used in the simulation and each beam has a waist of 1 mm and a peak amplitude 282 V/m , which is equivalent to intensity of 15.8 mW/cm^2 . Distance between their waist centers is 1.6 mm and propagation distance is 80 m. After 19 iterations the resulting intensity profile is converged and results are shown in Fig. 4-5(c). Periodic focusing and divergence of the two beams are again observed. Computation time for the iterative method and BPM are 3.9 minutes and 43 seconds. By comparing the results with the ones obtained by BPM, which is shown in Fig. 4-5(d), it can be seen that they are in a good agreement.

In this second example, evolution of intensity difference between two consecutive iterations is illustrated (Fig. 4-6). The difference becomes smaller when the iterations

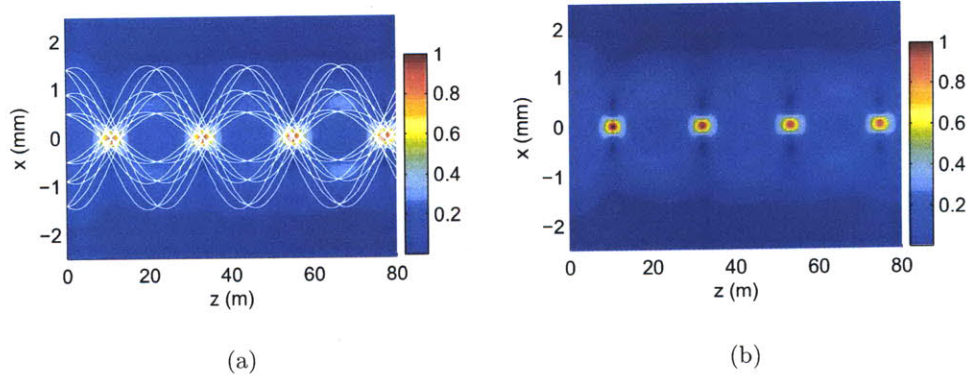


Figure 4-5: Periodic self-focusing of two Gaussian beams in Kerr medium produced by the iterative method (a) and BPM (b). The white lines are a subset of all 10100 rays used in the simulation. The color shading represents intensity, computed as projection along the momentum direction from the generated WDF.

continue. The intensity converges after 19 iterations and the results provide the beam propagation in nonlinear medium.

4.2.2 Spatial soliton

Spatial soliton happens when the effects as a result of diffraction and nonlinearity cancel with each other and the beam neither expand nor focus. It keeps on its shape as it propagates, resulting in a soliton. Analytical solution can be obtained for spatial soliton from the $(1 + 1)$ -dimensional NLS equation. Firstly $(1 + 1)$ -dimensional NLS equation is rewritten as

$$2in_0k_0 \frac{\partial A}{\partial z} + \frac{\partial^2 A}{\partial x^2} + 2k_0^2 n_0 n_2 I A = 0. \quad (4.6)$$

One solution of the NLS equation [54] is

$$A(z, x) = \sqrt{I_0} \operatorname{sech}(x/w_0) \exp(iz/2k_0 n_0 w_0^2) \quad (4.7)$$

where w_0 is the waist of light beam and $I_0 = (k_0^2 n_0 n_2 w_0^2)^{-1}$ is the peak intensity. This is the solution for the spatial soliton. It can be seen from the analytical solution that

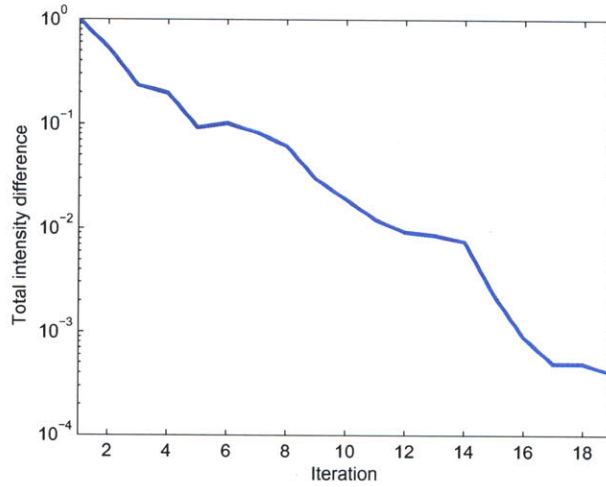


Figure 4-6: Total intensity difference between one iteration and its previous iteration.

it does not change its shape in x direction for different propagating position along optical axis z .

In this example, the illuminating source is the spatial soliton profile along x direction with $w_0 = 0.55$ mm and a peak amplitude $A = 281$ V/m, which equivalent to intensity of 15.7 mW/cm². The material parameters are the same as in the previous example. The estimates of the intensity profile converge after 16 iterations, and result is shown in Fig. 4-7 and Fig. 4-8(a). In Fig. 4-8(b)(c), the computed intensity profile is compared with the analytical result, which shows good agreement of the two results. Simulation time for iterative method is 3.1 minutes. A subset of rays used in calculation is shown in Fig. 4-8(a) to give a ray picture of the soliton. Interestingly, each ray follows an oscillating trajectory with different period. Rays with different initial positions and momenta carry different generalized radiances, and their trajectories are of different periods. They add up into a spatial soliton intensity profile. This is a very interesting ray picture for the spatial soliton.

4.2.3 Gaussian-Schell Model

As have been mentioned above, iterative nonlinear beam propagation method is based on the WDF, which means that it is also valid for partially coherent light illumination.

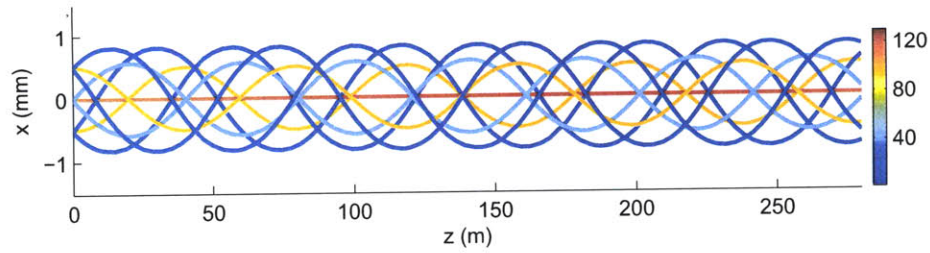
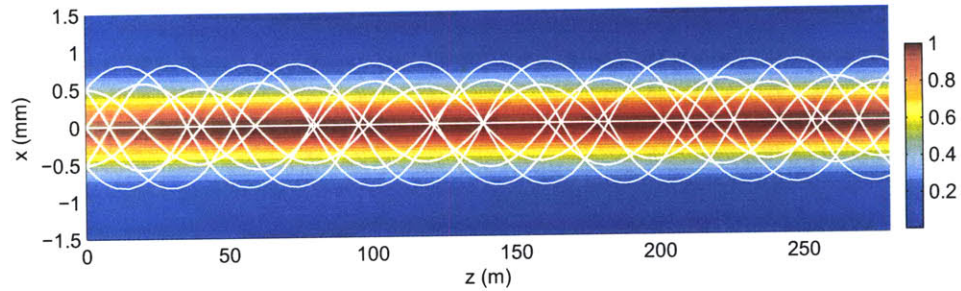
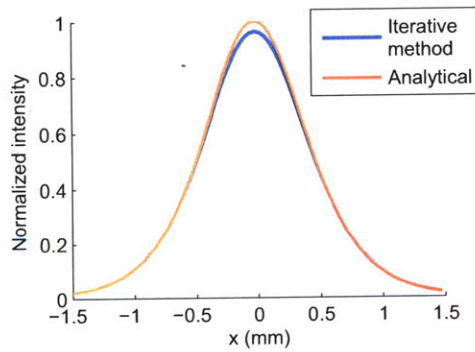


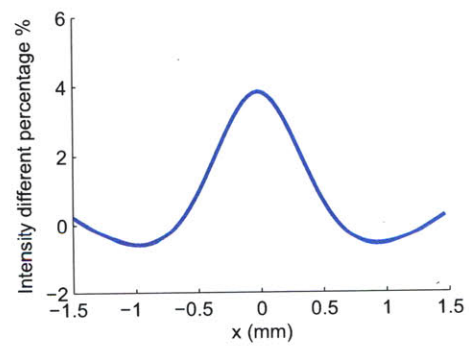
Figure 4-7: Ray tracing results from iterative nonlinear beam propagation method for spatial soliton. Lines are sampled from the ray tracing results and colors of rays indicate the generalized radiances carried by them based on WDF.



(a)



(b)



(c)

Figure 4-8: (a) Spatial soliton in Kerr medium produced by the iterative nonlinear beam propagation method and a subset of all 10100 rays used in the simulation. (b) Comparison of intensity distribution along x direction between the results from iterative method and analytical solution. (c) Intensity difference in percentage of spatial soliton along x direction between iterative method and analytical solution.

In order to validate this, Gaussian-Schell model is taken as an example for partially coherent regime.

Gaussian-Schell model is an ideal partially coherent light model in which both the intensity and the spatial coherent function follow the Gaussian distribution function. Its correlation function could be written as [12]

$$\Gamma(x_1, x_2) = \frac{\sqrt{2\sigma}}{\rho} \exp\left(-\frac{\pi}{2\rho^2} \left[\sigma(x_1 + x_2)^2 + \frac{1}{\sigma}(x_1 - x_2)^2\right]\right), \quad (\rho > 0, 0 < \sigma \leq 1) \quad (4.8)$$

where ρ is a scaling factor and σ is a measure of coherence. While $\sigma = 1$ corresponds to completely coherent light, $\sigma \rightarrow 0$ leads to incoherent light. The WDF of the Gaussian-Schell model has the analytical form which could be used in the iterative method is

$$\mathcal{W}(x, u) = 2\sigma \exp\left[-\sigma\left(\frac{2\pi}{\rho^2}x^2 + \frac{\rho^2}{2\pi}u^2\right)\right], \quad (\rho > 0, 0 < \sigma \leq 1), \quad (4.9)$$

where u is the spatial frequency related to the optical momentum. Interestingly, the WDF also follows the Gaussian distribution both in x and in u .

Eq. 4.8 could be rewritten by replacing $\bar{x} = (x_1 + x_2)/2$ and $\Delta x = x_1 - x_2$ and further parameter manipulation into

$$\Gamma(\bar{x}, \Delta x) = I_0 \exp\left(-\frac{\bar{x}^2}{a_0^2} - \frac{(\Delta x)^2}{l_c^2}\right), \quad (4.10)$$

where a_0 and l_c correspond to the width and correlation of the beam, respectively.

In this example, Gaussian-Schell model [96] with input beam width $a_0 = 25 \mu\text{m}$ and correlation length $l_c = 1.5 \mu\text{m}$ is examined. Fig. 4-9(a) shows the converged intensity profile of Gaussian-Schell model propagation in weak Kerr effect medium after 5 iterations. The beam width evolution is consistent with Eq. 4 of [96]. The full width at half maximum (FWHM) change in the case of $l_c = 1 \mu\text{m}$ and $2 \mu\text{m}$ is illustrated in Fig. 4-9(b). The results show good agreement with Fig. 1 of [96].

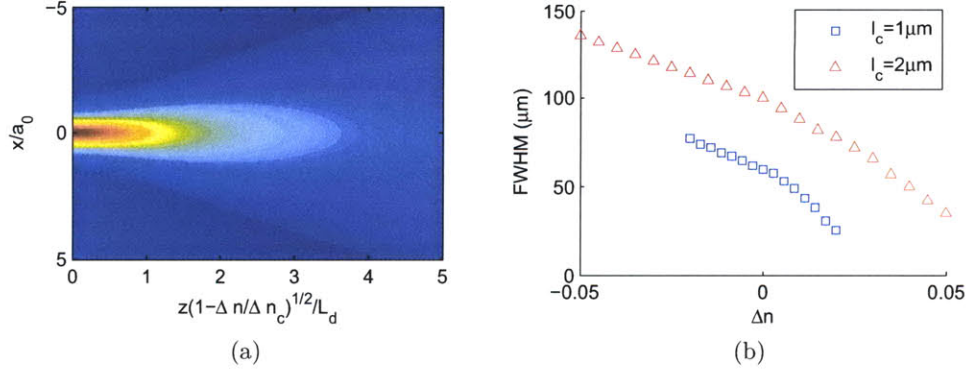


Figure 4-9: (a) Converged intensity profile for Gaussian-Schell model beam propagation in weak Kerr effect medium. (b) FWHM at different Δn for a fixed propagation length.

4.2.4 Ray diagrams of spatial solitons

Based on the results shown in Section 4.2.2, rays in spatial solitons follow oscillating patterns with different periods and they add up into solitons. It is interesting to investigate more properties of the ray diagrams of spatial solitons in detail.

Here the governing equations for ray tracing are derived based on Hamiltonian equations at the first place. Since the spatial soliton is stable so that the refractive index distribution of the nonlinear medium is stable and totally determined by the intensity profile of the soliton. Therefore, the index profile of the nonlinear medium is given as: $n = n_0 + n_2 \text{sech}^2(x/w)$. In this way, the ray tracing can also be found by treating the medium as linear but with the index profile given above. Ray tracing on the medium gives the right results.

Screen Hamiltonian equations are

$$\frac{dx}{dz} = \frac{\partial h}{\partial p_x} = \frac{p_x}{\sqrt{n^2 - p_x^2}} = -\frac{p_x}{h}, \quad (4.11)$$

$$\frac{dp_x}{dz} = -\frac{\partial h}{\partial x} = \frac{n}{\sqrt{n^2 - p_x^2}} \frac{\partial n}{\partial x} = -\frac{n}{h} \frac{\partial n}{\partial x}, \quad (4.12)$$

where the screen Hamiltonian is $h = -\sqrt{n^2 - p_x^2} = -p_z$.

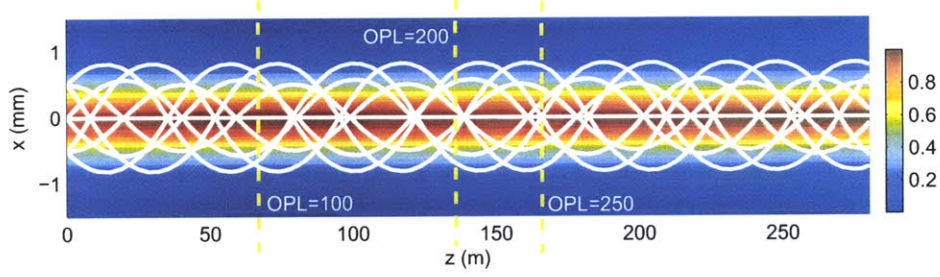


Figure 4-10: Hamiltonian ray tracing description of spatial soliton. White lines are sampled rays from the ray tracing results. Color shading denotes the distribution of normalized nonlinear index change $n_2I(x)$, i.e. intensity profile. Yellow dashed lines are the wavefronts for specific OPLs.

Therefore

$$\frac{d^2x}{dz^2} = -\frac{1}{h} \frac{dp_x}{dz} = \frac{n}{h^2} \frac{\partial n}{\partial x}. \quad (4.13)$$

Finally the equation governing the ray trace can be written as:

$$\frac{d^2x}{dz^2} = \frac{n}{h^2} \frac{\partial n}{\partial x} = \frac{n}{p_z^2} \frac{\partial n}{\partial x} = -\frac{n}{p_z^2} \cdot n_2 \cdot 2 \cdot \operatorname{sech}^2\left(\frac{x}{w}\right) \cdot \tanh\left(\frac{x}{w}\right) \cdot \frac{1}{w}. \quad (4.14)$$

where $n_0 = 1.5$, $n_2 = 2 \times 10^{-13} \times 281^2$, $w = 0.55 \times 10^{-3}$, which is the same as the soliton case above in Section 4.2.2. Numerically solving this equations gives out the oscillation results with different periods too.

The ray tracing results are shown in Fig. 4-10, which are consistent with the results obtained directly from the nonlinear beam propagation method (Fig. 4-8). In addition, the wavefronts are shown as yellow dashed lines by connecting the points with the same OPL. Wavefronts are vertical to the optical axis, which is in agreement with the analytical expression of spatial soliton, i.e. Eq. 4.7, where the phase only changes along z direction and keeps constant along x direction.

As expected, based on the ray tracing results, the generalized radiances of all the rays add up to the correct intensity profile of spatial soliton, even though most of them propagate in oscillatory fashion instead of straight lines parallel to the optical axis. More investigation is done on the WDF generated at different z planes. In Fig. 4-11, the calculated WDFs are illustrated. According to it, the WDF remains invariant

along the optical axis, which matches the Hamiltonian ray tracing description and also the analytical results. Furthermore, intensities at different z planes are calculated and illustrated in Fig. 4-12. From this figure it can be observed that the intensity is also invariant based on the iterative nonlinear ray tracing method results, maintaining the shape of spatial soliton while propagating. This ray picture provides an alternative description of soliton propagation with intuitive physical insight.

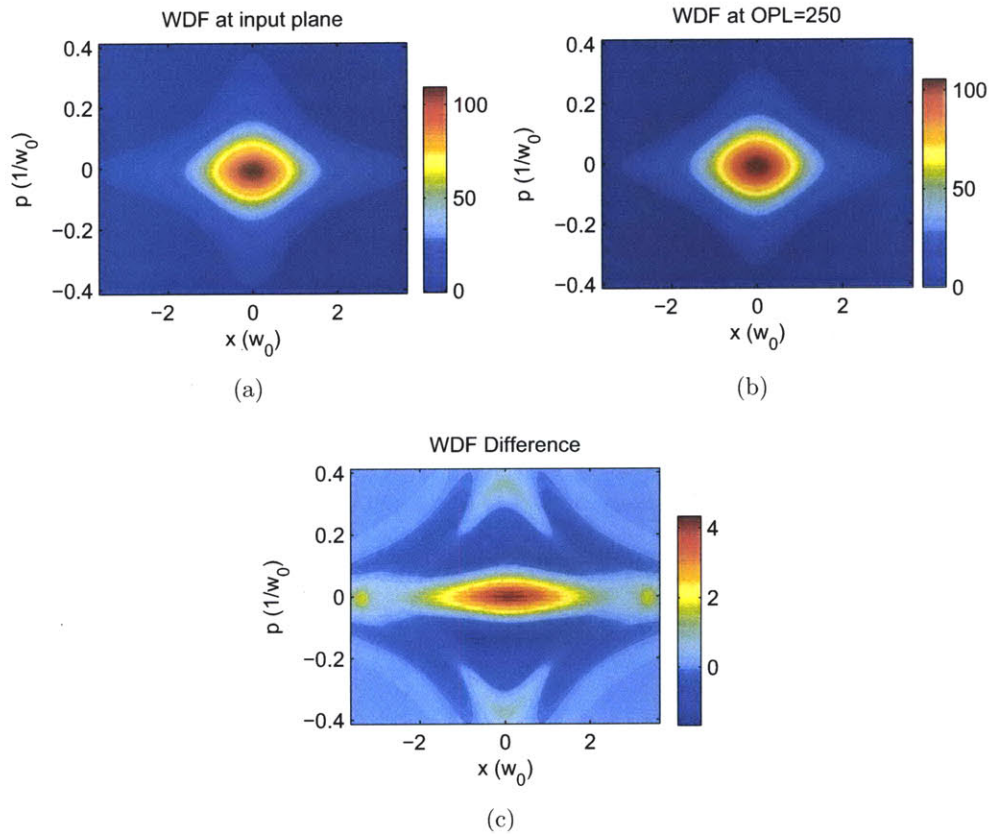


Figure 4-11: (a) WDF at the input plane. (b) WDF at the plane where OPL= 250. (c) The difference between (a) and (b).

4.3 Conclusion

In this Chapter, iterative nonlinear beam propagation method is introduced and validated with self-focusing and spatial soliton in coherent regime, and with Gaussian-

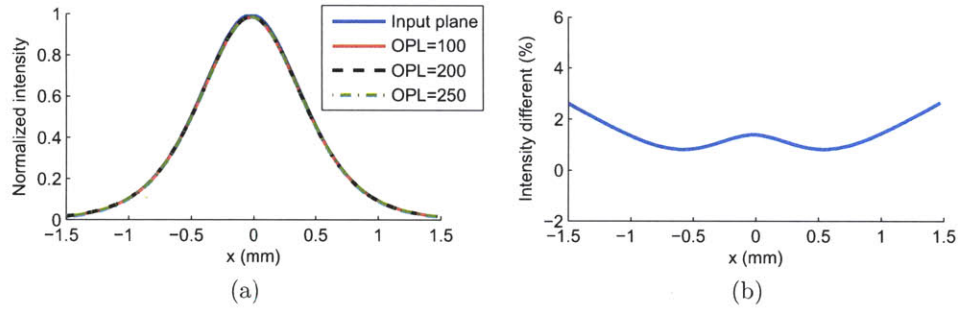


Figure 4-12: (a) Intensity distributions at different z planes. (b) The intensity difference between input plane and OPL= 250 plane.

Schell model in the partially coherent regime. This method provides physically intuitive ray tracing results. Generated ray diagrams provide a good physical perspective of the generalized radiance evolution for beam propagation in nonlinear media. Besides, this method is able to solve beam evolution in partially coherent regime. Furthermore, it provides a systematic approach to the investigation of light propagation in nonlinear photonic crystals and metamaterials. When applied to optical system design software based on ray tracing, while dealing with nonlinear component, it could keep the analysis solely on ray tracing, avoiding the transition between waves and rays. This method is computationally efficient. Though the computation time is a bit longer than BPM, in terms of all the advantages discussed above, it is a good compromise.

Chapter 5

Subwavelength Lüneburg lens with nonlinear Kerr effect compensation

Photonic crystals and metamaterials are two important research topics recently. Many useful properties and applications have been investigated, such as complete three-dimensional bandgap [14], slow light [102], self-collimation [53], optical cloak [101, 35], and so on. Nonlinearity, as an addition parameter, has been added to many applications of photonic crystals and metamaterials, and a lot of new properties have been reported, for example, nonlinear light propagation in photonic lattices using optical induction [33, 25], nonlinear pulse propagation in optical fibers [7], microdevices with bistability using nonlinear photonic crystal fabrication [26], and beam propagation in nonlinear periodic potential with Wannier functions [3]. They show interesting optical properties introduced by nonlinearity. A systematic approach for investigation of beam propagation in nonlinear photonic crystals and metamaterials is important.

In this Chapter, following the iterative method introduced in the previous chapter, an aperiodic subwavelength Lüneburg lens is used as a application for this method [38, 37]. We show that this method provides a computationally efficient way to analyze nonlinear devices as compared with FDTD method. In addition, it is emphasized that nonlinear Kerr effect is able to compensate the focal point shift caused by the diffraction of Gaussian beam. Properties of this nonlinear Lüneburg lens on imaging applications are investigated.

5.1 The lens equation of Lüneburg lens

Lüneburg lens was firstly proposed by R. K. Lüneburg [61]. It is a spherically symmetric lens bearing the imaging property that it is able to focus an incoming plane wave into a geometrical perfect focal point at the opposite edge of the lens. Due to this property, it is widely used in applications such as antenna arrays [72], reflectors [59], optical cloaks [71], etc. Lüneburg lens has an inhomogeneous but isotropic refractive index distribution, which can be expressed as

$$n(r) = n_0 \sqrt{2 - (r/R)^2}, \quad (5.1)$$

where n_0 is the ambient index outside the lens, R is the radius of the lens, and r is the distance to the lens center.

It is helpful to derive the lens equation for Lüneburg lens under paraxial approximation. Following geometrical optics, the positions of first and second principle planes should be located at the first place.

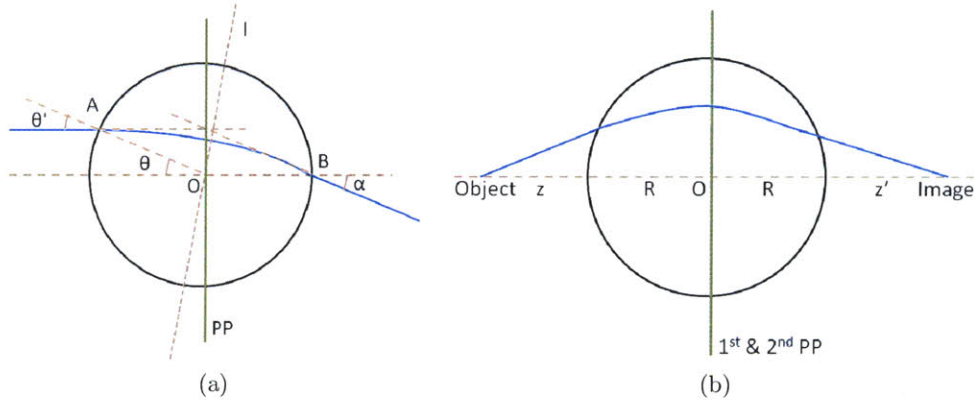


Figure 5-1: Derivation of lens equation for Lüneburg lens. (a) Determination of the primary and secondary principle planes. (b) Derivation of lens equation. Black circles enclose the Lüneburg lens, green vertical lines are the principles planes, and blue lines are sampled rays.

From Fig. 5-1(a), the principle planes (PP) could be determined. Blue line is a typical ray trace through the lens, where left of it is parallel to the optical axis (plane wave). It focuses at the right edge of the lens (Point B). Because of time reversal, if

we trace the ray backward, this blue line is also a valid ray trace. Due to the spherical symmetry of the Lüneburg lens, this trace should be symmetric to the Line l shown as the dashed line in Fig. 5-1(a). Thus the angles α and θ' are equal. Since $\angle\theta' = \angle\theta$, $\angle\alpha = \angle\theta$. By back extending the ray emanating out of the lens, it could be found that the secondary PP is located at the center of the lens. Accordingly, the primary PP is also located at the center of the lens.

With the positions of PPs on hand, lens equation can be derived. We assume that a point object is located at distance z to the left of the left edge of the lens, and image is located at distance z' to the right of the right edge of the lens. (Fig. 5-1(b)) The lens equation could be expressed as

$$\frac{1}{s} + \frac{1}{s'} = \frac{1}{f}, \quad (5.2)$$

where $s = z + R$, $s' = z' + R$ and $f = R$. This turns out to be

$$zz' = R^2. \quad (5.3)$$

This is the lens equation of Lüneburg lens under paraxial approximation.

5.2 Aperiodic subwavelength Lüneburg lens

Perfect Lüneburg lens, as a GRadient-INdex (GRIN) structure, is not achievable in bulk media. Thus, in this Chapter, a 2D aperiodic subwavelength nanostructured Lüneburg lens [97, 37] is studied (Fig. 5-2). This structure has been introduced in Chapter 2 for the investigation of Hamiltonian ray tracing applied to photonic crystals and metamaterials. It consists of silicon rods ($n = 3.46$) centered at each square lattice with lattice constant $a_0 = \lambda/8$, where $\lambda = 1550$ nm is the free space wavelength. The rod radii profile is $a(r) = a_1\sqrt{2 - (r/R)^2} + a_2$, where $a_1 = 0.367a_0$, $a_2 = -0.101a_0$ and $R = 30a_0$. The ambient medium is air ($n = 1$). In this structure, each unit cell can be treated as an effective medium since the wavelength is much larger than the lattice constant. Therefore, effective refractive indices are locally-

modulated by controlling the radii of the rods, mimicking the Lüneburg lens index profile. Throughout this Chapter, our discussions are based on this 2D subwavelength aperiodic nanostructure example.

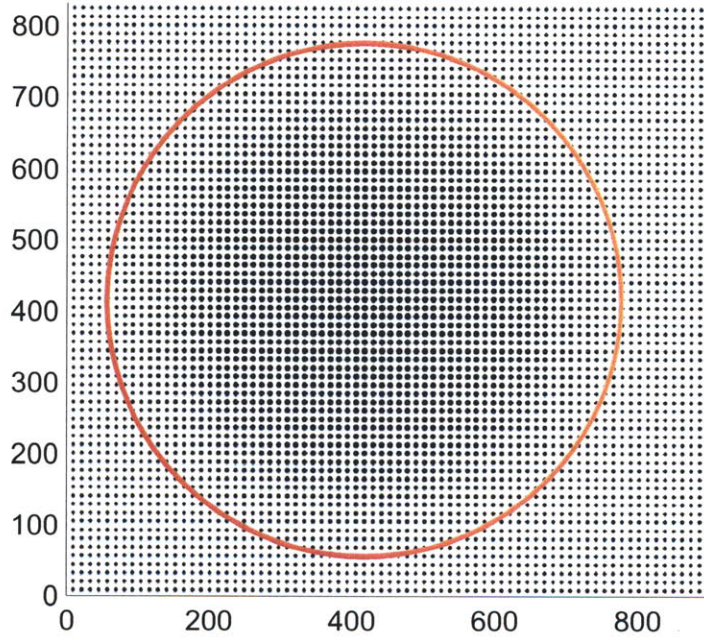


Figure 5-2: Subwavelength aperiodic nanostructured Lüneburg lens structure.

5.3 Nonlinear aperiodic subwavelength Lüneburg lens

As a lens, Lüneburg lens could focus the incoming plane wave into a perfect geometric focal point. However, in many cases, the object is not at infinity but at finite distance. Besides, Gaussian beams are more realistic models than plane waves. But in these two cases, the focal point will not be at the opposite edge but shifted outside the lens. In this way, the good property of Lüneburg lens vanishes. In this section, we claim that nonlinearity is able to compensate the focal shift and drive the focal point back

to the edge of the lens.

5.3.1 Setup

To validate this claim, a simulation setup is proposed, with a Gaussian beam input from the left of the lens and propagates out to the right, as illustrated in Fig. 5-3. The radius of the lens is R , and distances between the waist of input/output Gaussian beam and the left/right edge of the lens are z and z' , respectively.

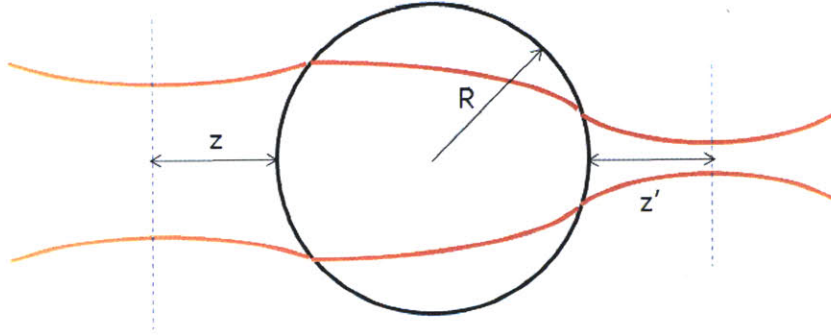


Figure 5-3: Simulation setup of nonlinear aperiodic subwavelength Lüneburg lens with a Gaussian source illumination. Black circle encloses the Lüneburg lens, and the red curved lines denote the profile of the Gaussian beam propagation. Blue dashed lines denote the waist of input/output Gaussian beams.

5.3.2 Simulation results

Nonlinear aperiodic subwavelength nanostructured Lüneburg lens is analyzed with both iterative nonlinear beam propagation method introduced in the previous chapter and FDTD. It has been shown in the previous chapters that the Hamiltonian ray tracing results and FDTD results are in good agreement. In this section, more emphasis is placed on the iterative method because this method is not only computationally efficient comparing with FDTD, but also provides ray diagrams which is physically more intuitive. In the following discussions, the FDTD is performed by the simulation software MIT Electromagnetic Equation Propagation (MEEP) [74].

First of all, we show that for a Gaussian beam illumination, the focal point will be shifted outside the lens without nonlinearity. In this simulation, a Gaussian beam

with beam width $36a_0$ and peak intensity I_0 (normalized) at the middle of the waist is illuminating the subwavelength Lüneburg lens from the left. Results are shown in Fig. 5-4. From it we see that in the linear Lüneburg lens case, a focal point shift to the right is obvious. The origin of the focal shift is the diffraction of the input Gaussian source as compared with the ideal plane wave source case. Therefore, for a Gaussian source input, the property of the Lüneburg lens that it has the geometrical focal point exactly at the opposite edge of the lens is invalid.

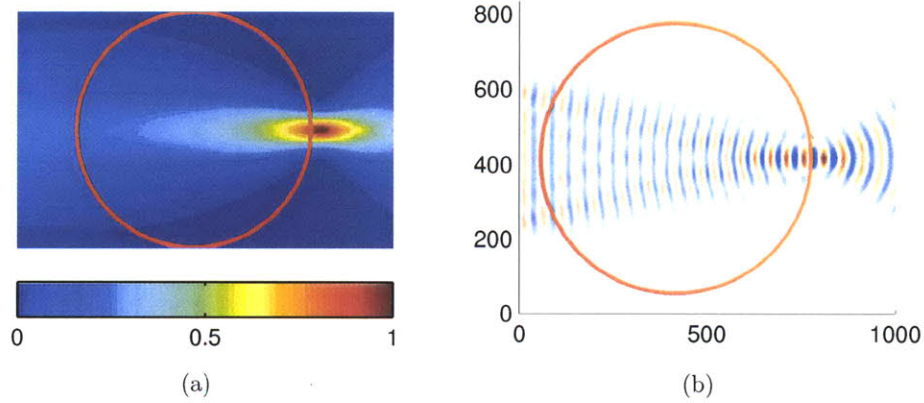


Figure 5-4: Linear aperiodic subwavelength Lüneburg lens with a Gaussian source illumination. (a) Intensity profile generated from nonlinear iterative beam propagation method (One iteration only). (b) Field distribution calculated based on FDTD method. Red circle encloses the Lüneburg lens.

Nevertheless, when taking Kerr nonlinearity into consideration, the results are different and are illustrated in Fig. 5-5. In this simulation, nonlinear Kerr coefficient for silicon is chosen as $2.7 \times 10^{-14} \text{ cm}^2/\text{W}$ [16]. For the iterative method simulation, grid size used is $0.03a_0 \times 0.03a_0$. After six iterations, the beam propagation profile converges. For the FDTD simulation, grid size is $0.083a_0 \times 0.083a_0$. By comparing this with previous results of Fig. 5-4, it can be seen that focal point is shifted back to the edge of the lens, thus the focal shift mentioned above has been compensated.

From all the discussions above, the Kerr nonlinearity could compensate the focal shift, which is a result of the competition between nonlinearity and diffraction. It is useful to discuss the reason why nonlinearity could counteract the diffraction in this

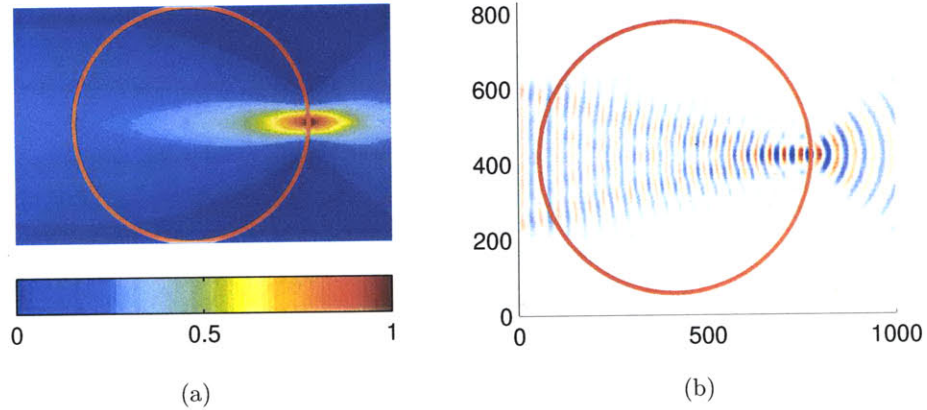


Figure 5-5: Nonlinear aperiodic subwavelength Lüneburg lens with a Gaussian source illumination. (a) Intensity profile generated from nonlinear iterative beam propagation method. (b) Field distribution calculated based on FDTD method. Red circle encloses the Lüneburg lens.

subwavelength Lüneburg lens case. In this lens, effective refractive index of certain unit cell is determined by the radius and refractive index of the cylindrical rod in it. Considering nonlinearity, the refractive index of the rod increases according to the local optical intensity. Therefore, the effective refractive index of the unit cell is higher than the linear case. The change of effective refractive index between linear and nonlinear Lüneburg lens is shown in Fig. 5-6, where two peaks can be clearly observed. The peak at the center of the lens is due to the relative larger radii of rods in these unit lattices. Assuming similar intensity, effective indices increase more for inner part of the lens than the outer part, since the rods near the center occupy more space in a unit cell. The other peak at the right edge of the lens is mainly caused by the high optical intensity near the focal point, meaning the refractive indices of the rods there are higher than others. In this way, effective refractive index gradient is increased in the nonlinear lens, and the rays will bend more towards the center and optical axis. Therefore, nonlinearity shifts the focal point by modifying the refractive index distribution of the lens.

Gutman has proposed the “modified Lüneburg lens” [44] which is able to change the focal point position by changing the Lüneburg profile, i.e. the refractive index

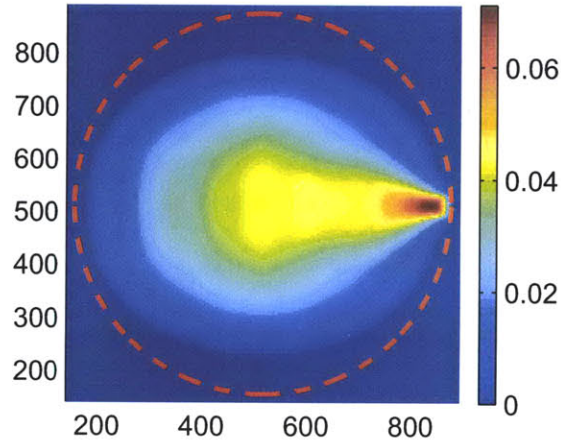


Figure 5-6: Effective refractive index difference between nonlinear and linear sub-wavelength aperiodic Lüneburg lens.

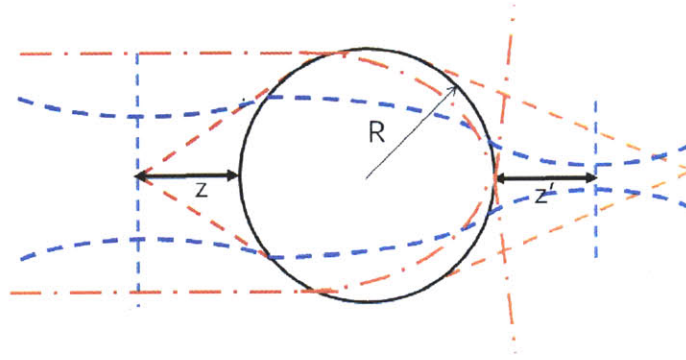
distribution. Refractive index difference shown in Fig. 5-6 should be compared with his “modified Lüneburg lens”. Here nonlinearity can be treated as a spherically symmetric perturbation to the refractive index, similarly shifting the focal point to the left (i.e. inside the lens.) The nonlinear refractive index change in our case is of the same order of magnitude with Gutman’s modified lens for the range of focal shifts considered; however, in our case the change is obviously not spherically symmetric, due to the high intensity in the focal region.

Based on this simple example, more cases are investigated to seek the relationship between the focal point positions, type of sources and optical intensities. Three types of sources, plane wave, point source and Gaussian source with various optical intensities, are discussed. The results are shown in Fig. 5-7. In this figure, for different types of sources considered, focal point position as a function of different source intensities has been illustrated. For plane wave illumination, which is an extreme case of Gaussian source with infinite large waist, as the intensity I approaches 0 (i.e. linear Lüneburg lens), focal point is at the opposite edge of the lens for the linear Lüneburg lens case. Increasing the intensity gradually shifts the focal point towards the center of the Lüneburg lens, as a result of higher Kerr nonlinearity. As the other extreme case of Gaussian source, the point source where the waist approaches zero

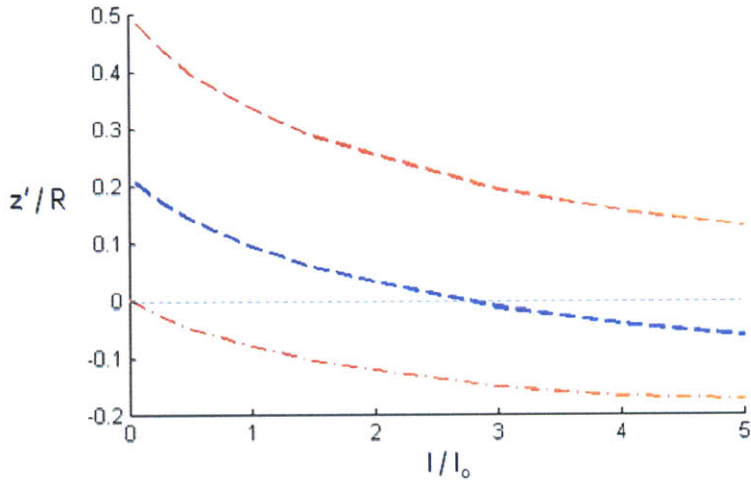
is also analyzed. Focal point without nonlinearity is at $z' = 0.5R$. This matches our geometric lens law for the Lüneburg lens: $zz' = R^2$, where $z = 2R$ and $z' = 0.5R$. As we increase the optical intensity, the focal point again moves towards the left, which is the same as in the case of the plane wave. However, since diffraction is too large to be compensated for this extreme case, it will not be back to the edge within the intensity range investigated here. Between the two extremes, the case with a Gaussian source of waist $9a_0$ is also calculated. From the figure, when $I = 2.8I_0$, focal position $z' = 0$, meaning that the nonlinear effect cancels the diffraction from the Gaussian beam. Further increase in intensity drives the focal point inside the lens. As a summary, for any Gaussian source illumination with a certain waist, diffraction could be compensated by Kerr effect nonlinearity when a proper optical intensity is chosen. Thus the focal point can be moved back to the edge of the lens.

5.4 Modified aperiodic subwavelength Lüneburg lens

One reason the iterative nonlinear beam propagation method is chosen is because it is able to provide ray diagrams which provide more physical insights into the beam evolution. Ray tracing results for the nonlinear Lüneburg lens have been shown in Fig. 5-8(a), where the input is a Gaussian source with waist size $125a_0$ and peak intensity I_0 . Generalized radiance evolution could be clearly seen. However, one problem appears. Fig. 5-8(a) shows a zoomed-in figure near the focal point and spherical aberration caused by nonlinearity is obvious. This aberration is mainly due to the intensity difference between the inner and outer part of the lens. For outer part, the intensity is lower, thus the effective refractive index increase is smaller. It results in low increase in refractive index gradient. For the inner part, refractive index gradient is higher. This could be seen from Fig. 5-6. Therefore, rays away from the optical axis bend less than those closer to the axis, causing the aberration. Focus positions for outer rays are to the right comparing with those of inner rays.



(a)



(b)

Figure 5-7: Relationship between focal point positions, source types and optical intensities. (a) Geometric setup with beam envelopes. (b) Focal point position (z') for different sources and intensities where $z = 2R$. Red dashed line: point source case; red dash-dot line: ideal plane wave case; blue dashed line: Gaussian source with waist $9a_0$. Horizontal blue line corresponds to the right edge of Lüneburg lens. Focal position z' is normalized to radius of lens R , optical intensity is normalized to I_0 .

Spherical aberration should be minimized for imaging. In this section, a modified aperiodic subwavelength Lüneburg lens is designed to meet this goal. An optimization method is used for the design. First a polynomial is used to describe the radii distribution of the rods:

$$R(r) = a_0 + a_1r + a_2r^2 + \dots, \quad (5.4)$$

where $R(r)$ is the radius of the rod at distance r from the center of the lens. The coefficients of the terms for the polynomial are treated as parameters in need of optimization in order to minimize the spherical aberration. Optimization results are shown in Fig. 5-9. From it we see that the inner part of the modified Lüneburg lens is almost the same as the original structure, while for outer part the radii of rods are lowered. This creates a higher effective refractive index gradient. Rays away from the optical axis will bend more to meet the focal point of inner rays. The ray tracing results generated from iterative nonlinear beam propagation method are illustrated in Fig. 5-8(b), where the spherical aberration has been minimized.

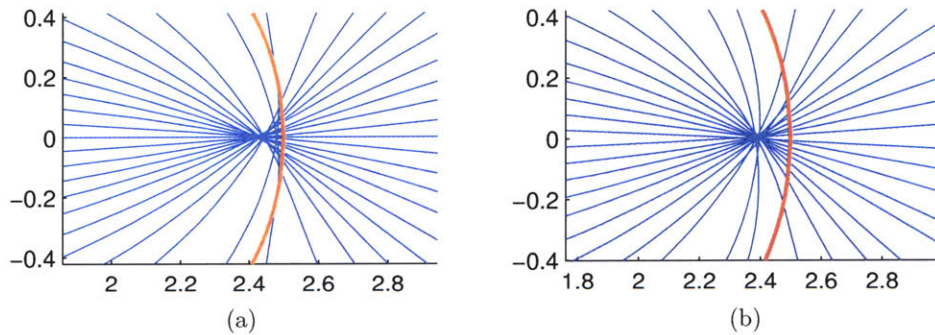


Figure 5-8: Spherical aberration minimization with the modified Lüneburg lens. (a) Ray tracing for nonlinear subwavelength Lüneburg lens. Spherical aberration can be clearly seen. (b) Ray tracing for the nonlinear modified Lüneburg lens. Spherical aberration has been minimized. The illuminating source is a Gaussian beam with waist $125a_0$ and peak intensity I_0 .

Nonlinearity causes change in focal point profile. Intensity profile cross sections at focal planes for the linear and nonlinear Lüneburg lens (see Fig. 5-4 and Fig. 5-5)

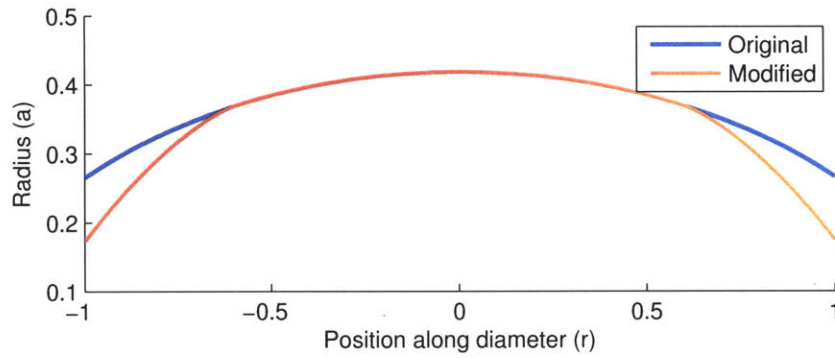


Figure 5-9: Rod radii distribution comparison for original and modified nonlinear Lüneburg lens.

have been shown in Fig. 5-10(a). The focal point is tightened a little. The change is not too much since spherical aberration is introduced for the nonlinear case. In addition, a comparison of focal points profiles for the original and modified Lüneburg lens (see Fig. 5-8) is illustrated in Fig. 5-10(b). It can be observed that the focal point is tightened, since the spherical aberration is minimized. The quality of focus is greatly improved.

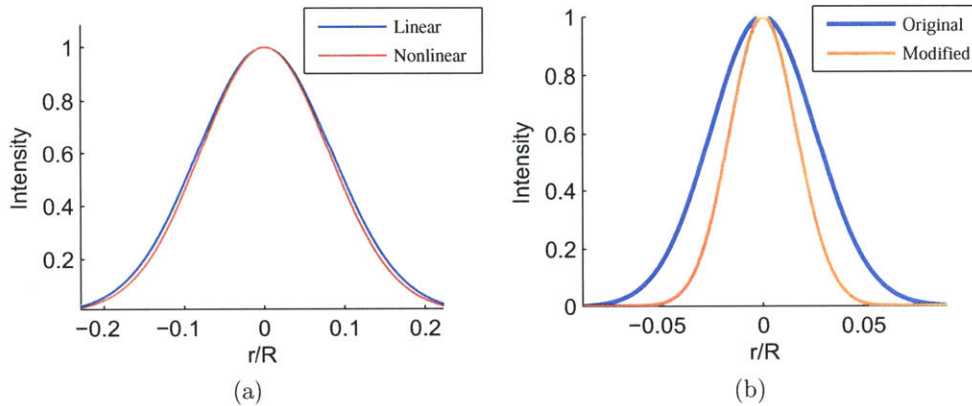


Figure 5-10: Change of focus point profile for original and modified subwavelength Lüneburg lens. (a) Comparison of focal point profile for linear and nonlinear subwavelength Lüneburg lens. (b) Comparison of focal point profile for original and modified nonlinear subwavelength Lüneburg lens.

5.5 Conclusion

In this Chapter, the iterative nonlinear beam propagation method has been applied to a nonlinear aperiodic subwavelength nanostructured Lüneburg lens. This method is emphasized because it is computationally more efficient than FDTD method. It has been shown that focal shift caused by diffraction of Gaussian beam can be compensated by nonlinearity. By proper choice of optical intensity, the property of Lüneburg lens that it has a focal point at the edge of the lens could be preserved. Nonlinearity induces spherical aberrations. Here a modified Lüneburg lens was designed to minimize the aberration caused. Iterative nonlinear beam propagation method provides an approach to analyze coherent or partially coherent beam propagation in nonlinear photonic crystals and metamaterials.

Bibliography

- [1] V. M. Agranovich, Y. R. Shen, R. H. Baughman, and A. A. Zakhidov. Linear and nonlinear wave propagation in negative refraction metamaterials. *Physical Review B*, 69(16):165112, 2004.
- [2] G. Agrawal. *Nonlinear Fiber Optics*. Academic, 2001.
- [3] G. L. Alfimov, P. G. Kevrekidis, V. V. Konotop, and M. Salerno. Wannier functions analysis of the nonlinear Schrödinger equation with a periodic potential. *Phys.Rev.E*, 66(4):046608, Oct 2002.
- [4] L. Allen, M. P. Padgett, and N. B. Simpson. Optical tweezers and optical spanners with Laguerre-Gaussian modes. *Journal of Modern Optics*, 43(12):2485–2492, 1996.
- [5] M. Alonso. Radiometry and wide-angle wave fields. i. coherent fields in two dimensions. *Journal of the Optical Society of America A*, 18(4):902–909, 2001.
- [6] H. Altug and J. Vuckovic. Two-dimensional coupled photonic crystal resonator arrays. *Applied Physics Letters*, 84(2):161–163, 2009.
- [7] D. Anderson. Variational approach to nonlinear pulse propagation in optical fibers. *Phys.Rev.A*, 27(6):3135–3145, Jun 1983.
- [8] P. K. Banerjee. *The Boundary Element Methods in Engineering*. McGraw-Hill, 1994. 93013475.
- [9] M. J. Bastiaans. Transport equations for the Wigner distribution function. *Optica Acta*, 26(10):1265–1272, 1979.
- [10] M. J. Bastiaans. Transport equations for the Wigner distribution function in an inhomogeneous and dispersive medium. *Optica Acta*, 26(11):1333–1344, 1979.
- [11] M. J. Bastiaans. The Wigner distribution function and Hamilton’s characteristics of a geometric-optical system. *Optics Communications*, 30:321–326, 1979.
- [12] M. J. Bastiaans. Application of the Wigner distribution function to partially coherent light. *Journal of the Optical Society of America A*, 3(8):1227–1238, 1986.

- [13] T. A. Birks, J. C. Knight, and P. S. J. Russell. Endlessly single-mode photonic crystal fiber. *Optics Letters*, 22(13):961–963, 1997.
- [14] A. Blanco, E. Chomski, S. Grabtchak, M. Ibisate, S. John, S. W. Leonard, C. Lopez, F. Meseguer, H. Miguez, and J. P. Mondia. Large-scale synthesis of a silicon photonic crystal with a complete three-dimensional bandgap near 1.5 micrometres. *Nature*, 405(6785):437–440, 2000.
- [15] M. Born and E. Wolf. *Principles of Optics*. Cambridge University Press, 2000.
- [16] R. Boyd. *Nonlinear Optics (3rd ed.)*. Academic, 2008.
- [17] J. Bravo-Abad, S. Fan, S. G. Johnson, J. D. Joannopoulos, and M. Soljačić. Modeling nonlinear optical phenomena in nanophotonics. *J. Lightwave Technol.*, 25:2539–2546, 2007.
- [18] D. A. G. Bruggeman. Berechnung verschiedener physikalischer konstanten von heterogenen substanzen. i. dielektrizitätskonstanten und leitfähigkeiten der mischkörper aus isotropen substanzen. *Annalen der Physik*, 416(7):636–664, 1935.
- [19] H. A. Buchdahl. *An introduction to Hamiltonian optics*. Cambridge University Press, 1970.
- [20] B. Chaudhury and S. Chaturvedi. Comparison of wave propagation studies in plasmas using three-dimensional finite-difference time-domain and ray-tracing methods. *Physics of Plasmas*, 13:123302, 2006.
- [21] X. Chen, T. M. Grzegorzczuk, B. I. Wu, J. Pacheco Jr, and J. A. Kong. Robust method to retrieve the constitutive effective parameters of metamaterials. *Physical Review E*, 70(1):16608, 2004.
- [22] R. Y. Chiao, E. Garmire, and C. H. Townes. Self-trapping of optical beams. *Physical Review Letters*, 13(15):479, 10/12 1964.
- [23] D. N. Christodoulides, T. H. Coskun, M. Mitchell, and M. Segev. Theory of incoherent self-focusing in biased photorefractive media. *Physical Review Letters*, 78(4):646–649, 1997.
- [24] D. N. Christodoulides, E. D. Eugenieva, T. H. Coskun, M. Segev, and M. Mitchell. Equivalence of three approaches describing partially incoherent wave propagation in inertial nonlinear media. *Physical Review E*, 63(3):35601, 2001.
- [25] D. N. Christodoulides, F. Lederer, and Y. Silberberg. Discretizing light behaviour in linear and nonlinear waveguide lattices. *Nature*, 424(6950):817–823, 2003.

- [26] M. Soljačić, C. Luo, J. Joannopoulos, and S. Fan. Nonlinear photonic crystal microdevices for optical integration. *Optics Letters*, 28(8):637–639, 2003.
- [27] M. Clemens and T. Weiland. Discrete electromagnetism with the finite integration technique. *Progress In Electromagnetics Research, PIER*, 32:6587, 2001.
- [28] H. Cory and C. Zach. Wave propagation in metamaterial multi-layered structures. *Microwave and Optical Technology Letters*, 40(6):460–465, 2004.
- [29] D. Dragoman. Wigner distribution function in nonlinear optics. *Applied Optics*, 35(21):4142–4146, 1996.
- [30] N. Engheta and R. W. Ziolkowski. *Metamaterials: Physics and Engineering Explorations*. Wiley-IEEE Press, 2006.
- [31] T. Ergin, N. Stenger, P. Brenner, J. B. Pendry, and M. Wegener. Three-dimensional invisibility cloak at optical wavelengths. *Science*, 328(5976):337, 2010.
- [32] Y. Fink, J. N. Winn, S. Fan, C. Chen, J. Michel, J. D. Joannopoulos, and E. L. Thomas. A dielectric omnidirectional reflector. *Science*, 282(5394):1679, 1998.
- [33] J. W. Fleischer, M. Segev, N. K. Efremidis, and D. N. Christodoulides. Observation of two-dimensional discrete solitons in optically induced nonlinear photonic lattices. *Nature*, 422(6928):147–150, 2003.
- [34] K. O. Friedrichs and J. B. Keller. Geometrical acoustics. II. Diffraction, reflection, and refraction of a weak spherical or cylindrical shock at a plane interface. *Journal of Applied Physics*, 26(8):961–966, 1955.
- [35] L. H. Gabrielli, J. Cardenas, C. B. Poitras, and M. Lipson. Silicon nanostructure cloak operating at optical frequencies. *Nature Photonics*, 3(8):461–463, 2009.
- [36] H. Gao, L. Tian, and G. Barbastathis. Hamiltonian ray-tracing with Wigner distribution function for wave propagation in inhomogeneous media. In *Frontiers in Optics, OSA Technical Digest (CD)*, page FMI5. Optical Society of America, 2010.
- [37] H. Gao, S. Takahashi, L. Tian, and G. Barbastathis. Nonlinear Kerr effect aperiodic Lüneburg lens. In *Optical MEMS and Nanophotonics (OPT MEMS), 2010 International Conference on*, pages 179–180. IEEE, 2010.
- [38] H. Gao, S. Takahashi, L. Tian, and G. Barbastathis. Aperiodic subwavelength Lüneburg lens with nonlinear kerr effect compensation. *Optics Express*, 19(3), 2011.
- [39] H. Gao, L. Tian, B. Zhang, and G. Barbastathis. Iterative nonlinear beam propagation using Hamiltonian ray tracing and Wigner distribution function. *Optics Letters*, 35(24):4148–4150, 2010.

- [40] J. C. Maxwell Garnett. Colours in metal glasses, in metallic films, and in metallic solutions. II. *Philos. Trans. R. Soc. London*, 205:237–288, 1906.
- [41] T. Georges, R. Jones, and J. Riley. Simulating ocean acoustic tomography measurements with Hamiltonian ray tracing. *Oceanic Engineering, IEEE Journal of*, 11(1):58–71, 2002.
- [42] H. M. Gibbs, S. L. McCall, and T. N. C. Venkatesan. Differential gain and bistability using a sodium-filled Fabry-Perot interferometer. *Phys. Rev. Lett.*, 36(19):1135–1138, May 1976.
- [43] J. W. Goodman. *Introduction to Fourier Optics*. Roberts and Company Publishers, 2004.
- [44] A. S. Gutman. Modified Luneberg lens. *Journal of Applied Physics*, 25(7):855–859, 1954.
- [45] B. Hall, M. Lisak, D. Anderson, R. Fedele, and V. E. Semenov. Statistical theory for incoherent light propagation in nonlinear media. *Phys. Rev. E*, 65(3):035602, Feb 2002.
- [46] E. Hecht. *Optics*. Addison-Wesley, 2002.
- [47] H. J. W. M. Hoekstra. On beam propagation methods for modelling in integrated optics. *Optical and Quantum Electronics*, 29(2):157–171, 1997.
- [48] P. U. Jepsen, B. M. Fischer, A. Thoman, H. Helm, J. Y. Suh, R. Lopez, and R. F. Haglund Jr. Metal-insulator phase transition in a VO₂ thin film observed with terahertz spectroscopy. *Physical Review B*, 74(20):205103, 2006.
- [49] Yang Jiao, Shanhui Fan, and David A. B. Miller. Designing for beam propagation in periodic and nonperiodic photonic nanostructures: Extended Hamiltonian method. *Phys. Rev. E*, 70(3):036612, Sep 2004.
- [50] S. G. Johnson, A. Mekis, S. Fan, and J. D. Joannopoulos. Molding the flow of light. 3(6):38, 2001.
- [51] Joseph B. Keller. Geometrical theory of diffraction. *Journal of the Optical Society of America*, 52(2):116–130, 02/01 1962.
- [52] P. L. Kelley. Self-focusing of optical beams. *Physical Review Letters*, 15(26):1005, 12/27 1965.
- [53] Qian Kemao. Two-dimensional windowed Fourier transform for fringe pattern analysis: Principles, applications and implementations. *Optics and Lasers in Engineering*, 45(2):304–317, 2007.
- [54] Y. Kivshar and G. Agrawal. *Optical Solitons*. Academic, 2003.
- [55] J. A. Kong. *Electromagnetic Wave Theory*. EMW Publishing, 2000.

- [56] R. G. Kouyoumjian and P. H. Pathak. A uniform geometrical theory of diffraction for an edge in a perfectly conducting surface. In *IEEE Proceedings*, volume 62, pages 1448–1461, 1974.
- [57] K. S. Kunz and R. J. Luebbers. *The Finite Difference Time Domain Method for Electromagnetics*. CRC, 1993.
- [58] Jensen Li and J. B. Pendry. Hiding under the carpet: A new strategy for cloaking. *Physical Review Letters*, 101(20), 2008.
- [59] C. S. Liang, D. A. Streater, Jian-Ming Jin, E. Dunn, and T. Rozendal. A quantitative study of Luneberg-lens reflectors. *Antennas and Propagation Magazine, IEEE*, 47(2):30–42, 2005.
- [60] W. T. Lu and S. Sridhar. Superlens imaging theory for anisotropic nanostructured metamaterials with broadband all-angle negative refraction. *Phys.Rev.B*, 77(23):233101, Jun 2008.
- [61] R. K. Luneburg. *Mathematical Theory of Optics*. Brown U.P., 1944.
- [62] E. W. Marchand. Ray tracing in gradient-index media. *JOSA*, 60(1):1–2, 1970.
- [63] E. W. Marchand. Ray tracing in cylindrical gradient-index media. *Applied Optics*, 11(5):1104–1106, 1972.
- [64] J. C. Maxwell. *A Treatise on Electricity and Magnetism*. Clarendon Press, 1873.
- [65] J. W. McKown and R. L. Hamilton Jr. Ray tracing as a design tool for radio networks. *Network, IEEE*, 5(6):27–30, 2002.
- [66] A. Mekis, J. C. Chen, I. Kurland, S. Fan, P. R. Villeneuve, and J. D. Joannopoulos. High transmission through sharp bends in photonic crystal waveguides. *Physical Review Letters*, 77(18):3787–3790, 1996.
- [67] M. Mitchell, Z. Chen, M. Shih, and M. Segev. Self-trapping of partially spatially incoherent light. *Physical Review Letters*, 77(3):490–493, 1996.
- [68] M. Mitchell, M. Segev, T. H. Coskun, and D. N. Christodoulides. Theory of self-trapped spatially incoherent light beams. *Physical Review Letters*, 79(25):4990–4993, 1997.
- [69] D. T. Moore. Ray tracing in gradient-index media. *J.Opt.Soc.Am*, 65:451455, 1975.
- [70] D. T. Moore. Gradient-index optics: a review. *Applied Optics*, 19(7):1035–1038, 1980.

- [71] N. A. Mortensen, O. Sigmund, and O. Breinbjerg. Prospects for poor-man's cloaking with low-contrast all-dielectric optical elements. *Journal of the European Optical Society-Rapid publications*, 4, 2009.
- [72] H. Mosallaei and Y. Rahmat-Samii. Nonuniform Luneburg and two-shell lens antennas: radiation characteristics and design optimization. *Antennas and Propagation, IEEE Transactions on*, 49(1):60–69, 2001.
- [73] M. Notomi. Theory of light propagation in strongly modulated photonic crystals: Refractionlike behavior in the vicinity of the photonic band gap. *Physical Review B*, 62(16):10696–10705, 2000.
- [74] A. F. Oskooi, D. Roundy, M. Ibanescu, P. Bermel, JD Joannopoulos, and S. G. Johnson. MEEP: A flexible free-software package for electromagnetic simulations by the FDTD method. *Computer Physics Communications*, 181(3):687–702, 2010.
- [75] S. R. P. Pavani and R. Piestun. High-efficiency rotating point spread functions. *Opt. Express*, 16(5):34843489, 2008.
- [76] S. R. P. Pavani, M. A. Thompson, J. S. Biteen, S. J. Lord, N. Liu, R. J. Twieg, R. Piestun, and WE Moerner. Three-dimensional, single-molecule fluorescence imaging beyond the diffraction limit by using a double-helix point spread function. *Proceedings of the National Academy of Sciences*, 106(9):2995, 2009.
- [77] J. B. Pendry. Negative refraction makes a perfect lens. *Phys.Rev.Lett.*, 85(18):3966–3969, Oct 2000.
- [78] T.-C. Poon and T. Kim. *Engineering Optics with MATLAB®*. World Scientific, 2006.
- [79] E. G. Rawson, D. R. Herriott, and J. McKenna. Analysis of refractive index distributions in cylindrical, graded-index glass rods (grin rods) used as image relays. *Applied Optics*, 9(3):753–759, 1970.
- [80] Ana Leonor Rivera, Sergey M. Chumakov, and Kurt Bernardo Wolf. Hamiltonian foundation of geometrical anisotropic optics. *Journal of the Optical Society of America A: Optics and Image Science, and Vision*, 12(6):1380–1380, 1995. Compilation and indexing terms, Copyright 2009 Elsevier Inc.
- [81] P. S. J. Russel and T. A. Birks. Hamiltonian optics of nonuniform photonic crystals. *Lightwave Technology, Journal of*, 17; 17(11):1982–1988, 1999. ID: 1.
- [82] J. B. Scarborough. *Numerical Mathematical Analysis*. Johns Hopkins U. P., 1966.
- [83] Y. Y. Schechner, R. Piestun, and J. Shamir. Wave propagation with rotating intensity distributions. *Physical Review E*, 54(1):50–53, 1996.

- [84] D. Schurig, J. J. Mock, B. J. Justice, S. A. Cummer, J. B. Pendry, A. F. Starr, and D. R. Smith. Metamaterial electromagnetic cloak at microwave frequencies. *Science*, 314(5801):977, 2006.
- [85] A. Sharma, D. V. Kumar, and A. K. Ghatak. Tracing rays through graded-index media: a new method. *Applied Optics*, 21(6):984–987, 1982.
- [86] V. V. Shkunov and D. Z. Anderson. Radiation transfer model of self-trapping spatially incoherent radiation by nonlinear media. *Physical Review Letters*, 81(13):2683–2686, 1998.
- [87] A. Sihvola. *Electromagnetic Mixing Formulas and Applications*. The Institution of Electrical Engineers, 1999.
- [88] Y. Silberberg and I. Bar Joseph. Instabilities, self-oscillation, and chaos in a simple nonlinear optical interaction. *Phys. Rev. Lett.*, 48(22):1541–1543, May 1982.
- [89] R. Simon and G. S. Agarwal. Wigner representation of laguerre-gaussian beams. *Optics Letters*, 25(18):1313–1315, 2000.
- [90] Oleg V. Sinkin, Ronald Holzlöhner, John Zweck, and Curtis R. Menyuk. Optimization of the split-step Fourier method in modeling optical-fiber communications systems. *J. Lightwave Technol.*, 21(1):61, 2003.
- [91] D. R. Smith, J. B. Pendry, and M. C. K. Wiltshire. Metamaterials and negative refractive index. *Science*, 305(5685):788, 2004.
- [92] D. R. Smith, D. C. Vier, T. Koschny, and C. M. Soukoulis. Electromagnetic parameter retrieval from inhomogeneous metamaterials. *Physical Review E*, 71(3):36617, 2005.
- [93] G. H. Spencer and M. V. R. K. Murty. General ray-tracing procedure. *J. Opt. Soc. Am.*, 52(6):672–676, Jun 1962.
- [94] G. Strang. *Computational Science and Engineering*. Wellesley-Cambridge Press, 2007.
- [95] G. Strang, G. J. Fix, and D. S. Griffin. An analysis of the finite-element method. *Journal of Applied Mechanics*, 41:62, 1974.
- [96] C. Sun, D. V. Dylov, and J. W. Fleischer. Nonlinear focusing and defocusing of partially coherent spatial beams. *Optics Letters*, 34(19):3003–3005, 2009.
- [97] S. Takahashi, C. Chang, S. Y. Yang, and G. Barbastathis. Design and fabrication of dielectric nanostructured Luneburg lens in optical frequencies. In *Optical MEMS and Nanophotonics (OPT MEMS), 2010 International Conference on*, pages 179–180. IEEE, 2010.

- [98] M. Testorf, B. Hennelly, and J. Ojeda-Castañeda. *Phase-Space Optics: Fundamentals and Applications*. The McGraw-Hill, 2010.
- [99] M. Tsang, D. Psaltis, and F. G. Omenetto. Reverse propagation of femtosecond pulses in optical fibers. *Optics Letters*, 28(20):1873–1875, 2003.
- [100] J. Um and C. Thurber. A fast algorithm for two-point seismic ray tracing. *Bulletin of the Seismological Society of America*, 77(3):972, 1987.
- [101] Jason Valentine, Jensen Li, Thomas Zentgraf, Guy Bartal, and Xiang Zhang. An optical cloak made of dielectrics. *Nature Materials*, 8(7):568, 2009.
- [102] Y. A. Vlasov, M. O’Boyle, H. F. Hamann, and S. J. McNab. Active control of slow light on a chip with photonic crystal waveguides. *Nature*, 438(7064):65–69, 2005.
- [103] A. Walther. Radiometry and coherence. *J.Opt.Soc.Am*, 58:1256–1259, 1968.
- [104] M. Y. Wang, J. Xu, J. Wu, B. Wei, H. L. Li, T. Xu, and D. B. Ge. FDTD study on wave propagation in layered structures with biaxial anisotropic metamaterials. *Progress In Electromagnetics Research*, 81:253–265, 2008.
- [105] E. Wigner. On the quantum correction for thermodynamic equilibrium. *Physical Review*, 40(5):749–759, 1932.
- [106] E. Wolf. Coherence and radiometry. *J.Opt.Soc.Am*, 68:6–17, 1978.
- [107] K. B. Wolf. *Geometric Optics on Phase Space*. Springer, 2004.
- [108] B. I. Wu, W. Wang, J. Pacheco, X. Chen, T. M. Grzegorzczuk, and J. A. Kong. A study of using metamaterials as antenna substrate to enhance gain. *Progress In Electromagnetics Research*, 51:295–328, 2005.
- [109] B. I. Zel’dovich, N. F. Pilipetskii, and V. V. Shkunov. Principles of phase conjugation. In *Berlin and New York, Springer-Verlag (Springer Series in Optical Sciences. Volume 42), 1985, 262 p.*, volume 42, 1985.
- [110] B. Zhang, T. Chan, and B. I. Wu. Lateral shift makes a ground-plane cloak detectable. *Physical Review Letters*, 104(23):233903, 2010.